AN EXPERIMENTAL INVESTIGATION OF

CONFINED VORTEX PHENOMENA

by

Benjamin M. Wei

A

Dissertation

in the

Faculty of Engineering

Presented in partial fulfilment of the requirements for the

Degree of MASTER OF ENGINEERING

at

Sir George Williams University

Montreal, Canada

March 1971

Benjamin M. Wei

AN EXPERIMENTAL INVESTIGATION OF

CONFINED VORTEX PHENOMENA

ABSTRACT

A 10-inch vortex chamber was built based on the concept of a vortex amplifier. Detailed measurements of the velocity profile at the exit plane of the vortex revealed strong reverse axial flow near the chamber axis, and the interdependency of this phenomenon with tangential input momentum. Radial velocity distribution indicated the existence of four counter-rotating Taylor-Görtler vortex rings. These rotating motions of the rings are superimposed on the vortex spiralling exit flow pattern.

The experimental results provide a better understanding of the complex flow configuration associated with high swirl vortex phenomena. Some of the findings are of significant importance in the design of devices utilizing vortex motions.

ACKNOWLEDGEMENTS

TABLE OF CONTENTS

LIST OF FIGURES.

NOMENCLATURE

a	cross-sectional area of probe
A	flow area of exhaust port
P_1	indicated total pressure
P_2	indicated static pressure
P_3	indicated static pressure
P_4	pitch angle pressure
P_5	pitch angle pressure
P_t	true total pressure
P_s	modified static pressure
P_{s1}	true static pressure
Re	Reynolds Number
R	radius of concave surface
$r, \emptyset, z$	cylindrical coordinate
V	velocity
$V_r, V_\emptyset, V_z$	radial, tangential and axial velocity components in cylindrical coordinate
ρ	fluid density
ψ	yaw angle
θ	pitch angle
$\ominus$	momentum thickness

CHAPTER 1

INTRODUCTION

In recent years, a great many practical applications have been evolved utilizing vortex flow phenomena. This is especially evident in the fields of heat transfer, combustion, meteorology and in the chemical industry. With the emergence of fluid controls as an upcoming technology, many ingenious ideas and fascinating concepts have generated further interest in the many possible applications of confined vortex motion.

Over the past hundred years, a vast amount of information on swirling flow phenomena has accumulated. The literature has been exhaustively reviewed and analyzed by many people prominent in the field, notably Donaldson and Sullivan [1], Gartshore [2] and Kwok [3]. Most of the earlier work is concerned with theoretical solutions of the Navier-Stokes equations using either approximate or numerical methods. In the former case, solution of the highly non-linear characteristics of these equations can only be obtained if greatly simplified assumptions are made. Therefore the results will be applicable only to special cases where such assumptions are valid. As a result, there

is no approximate mathematical model in existence capable
of completely describing complex vortex flow phenomena.

With advances in computer technology, the method
of solving the Navier-Stokes equations numerically has
gained preference over the approximate solutions where the
technique of perturbation and subsequent linearization of
the resulting equations were generally used. However, even
with the solution of the Navier-Stokes equations, very few
of the analytical results can be used for the design of
actual devices utilizing vortex phenomena.

The majority of the previous analytical work
developed the vortex flow model by either assuming an
inviscid flow or by using a viscosity whose value is equi-
valent to that of a laminar flow. In many practical
devices (i.e. vortex atomizers, vortex amplifiers) where
vortex motion is utilized, jets of fluid are generally
introduced tangentially at the peripheral wall of the
circular vortex chamber. This resembles flow along concave
walls where the destabilizing effects of centrifugal forces
create Taylor-Görtler vortices along the flow path. Accor-
ding to Schlichting [4], transition from laminar to turbu-
lent flow will occur almost immediately near the inlet for
a jet of sufficient strength. More specifically, when

$Re\sqrt{\Theta}/R > 7$, where Θ is the momentum thickness and R is the radius, transition from laminar to turbulent flow takes place. Since most of the practical devices will have $Re\sqrt{\Theta}/R$ much larger than 7, it is quite understandable that previous elaborate analytical solutions of the Navier-Stokes equations based on laminar flow viscosity are not applicable.

In turbulent flow, the pattern of streamlines at a fixed point fluctuates continually. This subsidiary motion causes an exchange of momentum in a direction normal to the flow because each particle has a tendency to substantially retain its momentum in the forward direction while mixing is taking place. In other words, the actual flow parameters in turbulent flow will be very different from those of laminar flow. However, the degree of turbulence is difficult to measure and almost impossible to predict. It also varies depending on the flow conditions and geometric configurations of the device under consideration.

It is felt, therefore, that further analytical studies of confined vortex flow phenomena at this stage will not be really meaningful unless the degree of turbulence within the vortex chamber can be accurately predicted. This is by no means a simple task since even now, after hundreds of papers have been published on subjects related directly or

indrectly to vortex motions, the complex flow mechanism is still not fully understood. Therefore, in order to acquire better physical insight into the flow field existing in a confined vortex chamber, further experimental investigations should be carried out.

Little literature is available on the results of detailed measurements of flow velocity profiles within the vortex chamber. Kelsall [5] used an optical method to measure the tangential, radial and axial velocity components by tracking fine aluminum particles at selected positions within a transparent hydraulic cyclone. In the early sixties, the experimental work on confined vortex flow was greatly intensified following the 1957 proposal by Kerrebrock and Meghreblian [6,7] of the cavity reactor concept for nuclear rocket propulsion and their 1959 vortex magneto-hydrodynamic power generator [8]. Williamson and McCune [9] conducted experimental measurements on a confined vortex chamber of aspect ratio from 0.13 to 0.281 (aspect ratio is defined as the ratio of chamber height to chamber diameter). They conducted axial traverse of the total pressure and calculated the radial distribution of tangential velocity based on these measurements.

Savino and Ragsdale [10] made measurements with a

pitot tube in a vortex chamber of aspect ratio 0.5 at
various radial and axial stations. Beverloo et al. [11]
made radial traverses of the total pressure within short
vortex chambers for a variety of injection ports, outlet
orifices and aspect ratios. The results provided informa-
tion on the radial distribution of tangential velocity
profiles only.

Kendall's experimental studies [12] investigated
vortex motions generated within a rotating porous ring which
induced a swirl to the fluid passing through it. The
cylindrical chamber had a diameter of 6 inches with an aspect
ratio of unity. Detailed traverse of the boundary layer
flow region was carried out using a flattened pitot probe
to determine flow direction as well as total pressure.
Although pitot probes are not very sensitive to flow
direction, Kendall's experimental measurements revealed some
interesting qualitative findings. His results indicated that
the maximum flow occurred at the measuring stations closest
to the solid boundary, and gradually decreased when moving
away from the wall.

Later, Donaldson and Williamson [13] made measure-
ments of the tangential and radial velocity components
within a cylindrical chamber of aspect ratio 0.167. The

fluid used was air injected through an outer porous ring and removed through a stationary concentric porous inner cylinder. Three basic measuring techniques were used: yaw probe to map the flow direction, pitot probe to measure the velocity, and hot wire probe to determine the mean fluctuating velocity components. The results indicated that the velocity distributions corresponded closely to those found by Kendall, except for minor discrepancies characterized by the different types of measuring instruments used.

An excellent paper was presented by Savino [14] who performed detailed experimental measurements of all velocity components and pressure distributions within a particular vortex chamber. The cylindrical chamber had a diameter of 11.72 inches and an aspect ratio of 0.107. Instead of the rotating porous ring to induce vortex flow used by previous investigators, 48 accurately aligned tangential guide vanes were used. Measurements were made at various stations along a diameter of the vortex chamber by means of a 3-tube pitot-yaw probe capable of accurately indicating both the total pressure and flow direction. The experiments were carried out at a velocity ratio of 10; velocity ratio is defined as the ratio of tangential velocity at the outer periphery to the radial velocity.

One of the more revealing experiments on confined vortex flow was reported by Kwok [3]. He measured not only the wall static pressure distributions of a vortex chamber of aspect ratio 0.02, but also conducted detailed measurements of the velocity profile at the exit plane of the central exhaust orifice. He compared the experimental measurements with his two-cell analytical model and found that strong reverse flow existed for confined vortex flow with high swirl, and that the apparent viscosity associated with the flow was of a magnitude some thousands of times greater than laminar viscosity.

More recently, Wormley [15] performed experimental investigations on a vortex chamber 7 inches in diameter. He used various flow visualization techniques to obtain qualitative information on flow patterns within vortex chambers under different velocity ratios. The results for high swirl conditions confirmed the findings of the previous investigators. Briefly, his findings indicated that at sufficiently high tangential inlet velocity, all the main flow is carried into the end wall boundary layer, while there is very little, or even reverse, flow in regions away from the boundary layer and in the middle section of the chamber.

Review of previous experimental work confirms the existence of secondary flow within high swirl vortex motions. This is why vortex phenomena are so complex and difficult to understand. However, most of the detailed measurements performed by the previous investigators have been concerned with the annular region inside the vortex chamber, whereas very little effort has been made to determine the vortex motion in the region around the central exit orifice, except for the work by Kwok.

Based on the amount of information available on velocity distributions within confined vortex chambers of small aspect ratio, it was thought that further detailed traversing of the vortex flow within such chambers would be repetitious. Furthermore, the physical limitations of the short, confined vortex chamber usually render experimental measurements more difficult. For example, a standard pitot probe, when introduced into a cylindrical chamber of, say, 0.20 inch in height, will create a disturbance of such magnitude that the originally intended measured flow pattern will be drastically affected and the results no longer meaningful. Instead, it was considered that effort should be devoted to further extending the work done by Kwok in measuring the exit velocity profiles of the confined vortex flow. It is believed that the results would provide better

physical insight into complex vortex flow phenomena.

The objectives of the present experimental study are the following:

(1) to design and fabricate a cylindrical chamber having a built-in arrangement for variation of aspect ratios and special controls to vary the input velocity ratios;

(2) to measure the wall static pressure distribution across the vortex chamber;

(3) to measure the velocity components at the exit plane of the central exhaust orifice and to critically discuss the experimental results.

The second and third objectives were carried out for flow in the same cylindrical chamber but with varying aspect and inlet velocity ratios.

CHAPTER 2

EXPERIMENTAL APPARATUS

In order to attain the stated objectives, it was first necessary to acquire three major pieces of apparatus:

(1) a cylindrical vortex chamber with built-in flexibility for adjustment of aspect ratio and for control of input velocity ratio;

(2) a probe capable of measuring both direction and velocity of the flow exhausting from the central orifice;

(3) a traversing mechanism providing a three-dimensional adjustment with linear movement accurate to .05 inch.

Each piece of apparatus is described in detail as to function, operating principle and design parameter.

2.1 Experimental Vortex Chamber

Most previous investigators generated their required vortex motions by either injecting the fluid through a rota-

ting porous cylinder [12,13], or using accurately-aligned guide vanes or nozzles oriented in a predetermined direction to induce the necessary swirl to the incoming fluid. The first method involves moving parts and therefore entails more complex design as well as mechanical or electrical power supply. The guide-vane approach, on the other hand, necessitates not only extreme accuracy in machining, but also allows only limited inlet flow conditions (i.e. velocity ratios) which are dependent on the geometrical configuration of the particular vane or nozzle arrangement. In an attempt to minimize the disadvantages presented by the two above-mentioned schemes, a vortex chamber was designed employing a concept similar to the vortex amplifier used in fluidic technology.

The general configuration of a vortex amplifier is shown schematically in Fig. 1. The radial supply flow, commonly referred to as the power flow, enters behind a circular plate and then passes around the plate into the vortex chamber. The incorporation of this circular plate is actually an improvement over the vortex amplifiers of earlier design. This configuration forces the supply flow to enter the vortex chamber through an annulus region in a uniform flow sheet. Control flow, which has a very strong tangential velocity component, generated in the control plenum

chamber and is introduced into the annulus at right angles to the flow. Even mixing of the two flows is accomplished by the use of several identical control flow injection ports located uniformly around the chamber wall. When mixing takes place, swirl is imparted to the supply flow by the tangential component of the control jets in the annulus.

As the "mixed" flow enters the vortex chamber and moves towards the central exhaust orifice, the tangential velocity of the flow increases because of the conservation of angular momentum. The centrifugal force thus generated opposes the upstream pressure and increases the flow resistance of the vortex amplifier. This is the basic operating principle of the vortex amplifier, and the vortex motion generated by the tangential control jets determines the throttling effect of the inlet supply flow. The reason for considering this device to be an amplifier is that a very small control flow injected tangentially into the chamber will throttle the much greater rate of the supply flow.

The vortex chamber used in our studies, and shown in Fig. 2, has a chamber diameter of 10 inches and a total of eight identical tangential nozzles 7/32 inch in diameter,

symmetrically placed along the periphery of the chamber. Special plugs permit blocking of some of the nozzles as desired. Pressurized air is fed through the supply inlet and the flow passes around the circular plate before entering the vortex chamber. The tangential nozzles impart a swirl component to the supply flow and the intensity of swirl is governed by the pressure in the control jet plenum chamber. Flow is discharged into the atmosphere through a central exhaust port. The exhaust port is designed so as to facilitate installation of different sizes of outlet as shown in Fig. 3. There are three interchangeable outlet ports of 1.0, 1.5 and 2.0 inches diameter. There are also three sets of "spacers", two of which are shown in Fig. 4. Interchanging of these spacers allows adjustment of the vortex chamber height from 0.375 to 1.00. In other words, experimental measurements may be conducted on vortex chambers of aspect ratios from 0.0375 to 0.100.

The end wall on the same side of the outlet port was fabricated with a total of 22 wall static pressure taps, arranged in the manner shown in Fig. 5. All the pressure taps were 1/16 inch diameter and were carefully machined with clean square edges to ensure validity of the experimentally measured pressure values.

2.2 Directional Probes

The major objective of this experimental study
is to measure accurately the velocity profiles at the exit
plane of the vortex exhaust core region. The flow leaving
the vortex chamber, as may be expected, is highly complex
in nature. In order to obtain the velocity vector, the
flow direction at any point must first be carefully deter-
mined. Previous work by Kwok utilized a simple yaw probe
to establish the yaw angles in two planes perpendicular
to each other by rotating the probe 90°. Once the correct
flow direction was found, the magnitude of the velocity
vector was computed from reading the pitot and static
probes measured separately at the same point with the same
angular orientation. The velocity vector was then resolved
into tangential, radial and axial components.

It can be seen that this procedure is not only
time-consuming, but also that the accuracy of the results
is open to question. Since the flow direction and magnitude
must be measured by separate probes, errors are likely
during changing and setting of the probes. Savino used
a 3-tube pitot probe which is very sensitive to yaw in
the plane of the tubes. Unfortunately, sensitivity to
pitch is very poor in this particular type of probe.

It was decided to use a five-hole 3-dimensional probe (United Sensor and Control Corp. model DA 125) for experimental studies. This probe has a five-hole, prism-shaped measuring section and is capable of measuring yaw and pitch angles, and static and total pressures. Detailed manufacturer's specifications, measurement procedures and calibration curves up to a pitch angle of 40° are presented in Appendix I. Special correction factors for measurement error in static pressure, yaw and pitch angles and, in particular, error due to the obstruction of flow passage by the measuring probe, are also described in the appendix.

The manufacturer furnished an individual calibration curve for pitch angles up to 40°. In the preliminary measurements of the vortex flow, it was realized that the pitch angle at certain measuring stations far exceeded the 40°-limit. As a result, recalibration of the probe was carried out. This exercise, although extremely time-consuming, provided not only a calibration chart extending the pitch angle limit to over 110°, but also confirmed the accuracy of the manufacturer's data. This calibration curve is presented in Fig. A.6 of Appendix I.

2.3 Traversing Mechanism

In the work by Kwok [3], an ingenious probe holder mechanism is described for measurements of the exit velocities of vortex flow. This device permits universal adjustment of the probe in practically any direction while maintaining the tip at a fixed point. In this investigation, however, a more advanced five-hole directional probe was used. This probe does not require such an elaborate set-up because once the tip position is accurately located, the measuring procedure necessitates only a small rotation of the probe on its axis to reach equal static pressure at two specific take-off tubes.

The Fluid Controls Group at Sir George Williams University has an excellent traversing system which was designed and built for the project on "Turbulence Measurement in the Velocity Field of a Three-Dimensional Air Jet". The apparatus, shown in Fig. 6, was used for the present experimental investigations.

The main traversing system permits movement in three dimensions with an accuracy of 0.05". A separate unit, mounted on the "Z" traverse axis, as seen in Fig. 6, has a probe-holder capable of additional three-dimen-

sional movement for space correlations. The accuracy of
this unit is approximately 0.0005". An adjustable disc
dial is fitted to the tip of the probe-holder which can
be rotated either in the horizontal or vertical plane.
Accuracy of the angular calibration of the dial is within
2°.

CHAPTER 3

TEST PROCEDURE AND DATA REDUCTION

General views of the experimental set-up with measuring instruments are shown in Figs. 6a and 6b. For a typical run, the supply flow rate must be adjusted, together with the control flow rate to the desired values. Error in flowmeter readings due to back pressure effects were carefully corrected using the manufacturer's recommended procedure. Twelve sets of results, covering supply flow rates of 10, 15 and 20 scfm, and control flow rates of 10, 15, 20 and 30 scfm were carried out. These results were obtained on the 10-inch diameter test chamber of aspect ratio 0.05 with a 2-inch diameter exhaust port. It should be noted that, although this vortex chamber was designed so that both its aspect ratio and exhaust port size could be varied over a large range, our experimental investigation concentrated only on the above-mentioned geometric configurations.

As is to be expected, it takes some time for flow to reach its steady condition, therefore precautions were taken so that at least five minutes elapsed to allow the flow, as well as the manometers, to reach steady state values. All

the wall static pressures were first fed through a junction box and then into a strain gauge type Pace pressure transducer. When it was later found that the results were not reproducible due to small leakages in the junction box, Meriam liquid-filled (S.G. 0.812) manometers were used. These manometers were easily readable to within 0.05 inch accuracy. The wall static pressure distributions provide further checks on the symmetry of the vortex motion under investigation.

A typical traverse was started by first aligning the probe in a horizontal plane by means of a transit and setting it 1/16 inch away from the exit plane of the exhaust port. The probe was then rotated until the pressure difference between the two yaw pick-off tubes (i.e. P_2 and P_3) shown in Fig. A.3 of Appendix I was zero. The yaw angle "ψ" of the flow velocity vector at the measuring point was then indicated on the dial of the traversing mechanism.

All the pressures, P_1, P_2, P_3, P_4 and P_5, from the five-hole directional probe, were recorded. Pitch angle θ was determined by calculating $(P_4 - P_5)/(P_1 - P_2)$ and using the calibration curves for the probe, such a curve A shown in Figs. A.4 and A.5 of Appendix I. Once the pitch angle was known, the velocity pressure coefficient $(P_t - P_s)/$

$(P_1 - P_2)$, and total pressure coefficient $(P_1 - P_t)/(P_t - P_s)$, could be read from curves B and C where P_t and P_s are total and static pressures respectively. With these two coefficients, P_t and P_s, as well as $(P_t - P_s)$, could be calculated.

The static pressure P_s found in this manner is subject to error in measurement because when a probe is introduced into the flow, the cross-sectional area of the flow is reduced and static pressure changes. In other words, the static pressure, P_s, measured will not be the same as the original flow static pressure P_{s1}. When this type of probe is placed perpendicular to the flow, the actual drop in static pressure at the probe cross-section and downstream from it is, approximately:

$$\frac{P_{s1} - P_s}{P_t - P_{s1}} = 1.2 \frac{a}{A} \qquad (1)$$

where a/A is the fraction of passage area A blocked by the cross-sectional area of probe a. Since P_s, P_t, a and A are all known, the true static pressure P_{s1} can be found from eq. (1).

Once the corrected total pressure P_t, static pressure P_{s1}, yaw and pitch angles (ψ, θ) are known, the

velocity vector V is determined using Bernoulli's equation

$$V = \sqrt{\frac{2(P_t - P_{s1})}{\rho}} \tag{2}$$

where ρ is the density of the fluid used. In this case, the fluid is air with density equal to 0.002378 slug/ft^3 under normal temperature and pressure conditions.

The velocity vector is then resolved into tangential, radial and axial components using the following relationships:

$$V_t = V \sin \psi \tag{3}$$

$$V_r = V \cos \psi \sin \theta \tag{4}$$

$$V_z = V \cos \psi \cos \theta \tag{5}$$

These relationships are shown diagrammatically in Fig. 7.

It should be noted that in the calibration data shown in Figs. A.4 and A.5, particularly the total pressure coefficient versus pitch angle curve "C", a small variation of the total pressure coefficient $(P_1 - P_t)/(P_t - P_s)$,

resulted in a large change in pitch angle, and vice versa. In order to improve the accuracy of interpretation of the calibration data, a piece-wise linearization technique was used. A computer programme was prepared whereby all the actual calibration data were fed into the computer memory core. Accurate interpretations of the pitch angle, velocity pressure and total pressure coefficients were then easily obtainable for any given set of measured pressure readings from the probe.

Another computer programme was written to evaluate the velocity components using eqs. (1) through (5). This programme, although basically very simple, saved considerable time in calculation of the experimental data. With the two above-mentioned programmes, all that is necessary is simply to process pressure readings from five-hole directional probe, together with the atmospheric conditions, into the computer which in turn will provide the required tangential, radial and axial velocity components of the flow. Any significant errors found can immediately be traced back to the original set of measured data. The aforementioned computer programmes are presented in Appendix II.

Repeatibility and accuracy of the experimental

measurements were checked by carrying out seven different
runs of one specific test condition using equal supply and
control flow rates of 10 scfm. The results are tabulated in
Appendix III where the standard deviations and coefficients
of variation* are presented. The maximum coefficient of
variation of the total velocity is about 8%.

---

*The measure of relative variation most commonly employed
is that developed by Pearson, termed the coefficient of
variation, which is simply the standard deviation as a
percentage of the arithmetic mean. This is described in
"Statistical Methods" by F.C. Mills.

CHAPTER 4

RESULTS AND DISCUSSION

A great many tests were conducted using the 10-inch vortex chamber of aspect ratio equal 0.05. Tests covered ranges of supply flow rates of 10, 15 and 20 scfm and control flow rates of 10, 15, 20 and 30 scfm. Tests on smaller flow rates were also carried out. The results generally follow trends similar to those of the higher flow rates, except that the phenomena indicated are not as strong for the particular vortex chamber geometric configuration. Therefore, these data are not presented.

All the experimental results are presented in Figs. 8 to 22 and are separated into two main groups for ease of discussion. The first group concerns the radial velocity distribution of the exit core flow for constant supply flow rate and different control flow rates. The second group shows constant control flow rates with different values of supply flow. It must be understood that the term "control flow" does not carry the connotation of a vortex amplifier. The control flow in this context actually represents the strength or magnitude of the angular momentum imparted to the vortex flow.

From the measured results, it can be seen that the points traversed do not include the area right up to the edge of the exit hole. This is due to the limitation of the five-hole directional probe used. It is stated by the manufacturer that all five holes of the probe, covering a width of approximately 1/8 inch, must be completely exposed to the flow in order to ensure accurate measurement. Therefore, no measurement was possible at stations near the edge of the exit hole.

Measurements in the vicinity of the centre of the vortex were attempted but the results were erratic and not repeatable. The velocity vector near or at the axis was assumed to be small since both the tangential and radial velocity components must approach zero. The introduction of a probe into this critical region will, in all likelihood, disturb the flow and severely affect the axial velocity. Furthermore, the exit core flow of such a vortex is not absolutely stable. Similar phenomena can be observed while watching water draining from a bathtub where the air core of the vortex moves randomly. The two factors mentioned above rendered detailed measurements of the region near the vortex axis extremely difficult and such measurements were not performed.

4.1 Experiments with Constant Supply Flow Rate and Different Control Flow Rates

4.1.1. Radial Distribution of Axial Velocity Component

Fig. 8 presents the radial distribution of axial velocity components for a constant supply flow rate of 10 scfm and three different values of control flow rate, 10, 20 and 30 scfm. It can be seen that with the high control flow rates used, the tangential momentum imparted to the flow is very significant. From the principle of conservation of angular momentum, the tangential velocity component is bound to increase as the fluid moves towards the centre. The increase in velocity results in a decrease in static pressure which finally reaches a level well below that of the ambient. When this happens, a column of air is sucked into the vortex flow along its centre-line. This reverse flow phenomenon is indicated by the negative axial velocity components near the axis of flow as shown in Fig. 8.

For higher control flow rates, the generation of low pressure is also intensified and the reverse flow area, where axial velocity components are moving in the direction opposite that of the main flow, is increased. This argument is well substantiated by the experimental results presented.

The results in Fig. 8 also indicate that for higher control flow rates the magnitude of the axial velocity components in both the positive (outward) and reverse flow directions are larger. This is explained by following the previous argument that the reverse flow area increases with higher control flow rate. Since these tests were conducted with a constant supply flow rate, any increase in control flow rate automatically increases the total input flow rate to the vortex chamber. In other words, all flow rates, including those entrained through the reverse flow region, would have to be forced out through an annular area which decreases in size with increasing total flow. The only way in which this can happen is to increase the positive axial velocity. This is precisely indicated by the experimental data. It is also interesting to note that the magnitude of the reverse axial flow component increases with increase of control flow rate. This is quite obvious since the static pressure reduces significantly near the core region when the control flow rate, or the tangential velocity component, is increased.

One finding, as seen in Fig. 8, reveals that when V_z equals zero, a maximum axial velocity gradient $(\partial V_z/\partial r)$ occurs. Even though no actual experimental measurement was taken in the vicinity of the edge of the exhaust hole, it

was expected that the axial velocity gradient would also be high. Since shear force is directly proportional to the velocity gradient, the axial shear stress will also approach its maximum near or at the point where the axial velocity component is equal to zero. Maximum shear force corresponds to maximum friction losses. The experimental findings reveal some very interesting phenomena which may be of value in connection with the extraordinary losses experienced in devices utilizing vortex flow.

4.1.2. Radial Distribution of Tangential Velocity
Component

Under the same flow conditions (i.e. supply flow
rate 10 scfm and control flow rates 10, 20 and 30 scfm), the
radial distributions of the tangential velocity components
in the exit plane of the exhaust hole are shown in Fig. 9.
The experimental curves indicate that, as control flow
rate is increased, a corresponding increase in tangential
velocity is realized. This is quite obvious since the
magnitude of the tangential velocity components should be
directly related to the input control flow rate.

The results also show that the magnitude of the
tangential velocity initially decreases very rapidly until
it reaches the region where axial reverse flow starts, at
which time the rate of change is drastically reduced as
the flow moves towards the centre. However, there is no
reversal of tangential flow direction in a manner analogous
to that of the axial flow shown in Fig. 8. In other words,
the swirl is always in the same direction as the control input
flow. The axial reverse flow discussed earlier, although
moving in a direction opposite that of the exhaust flow, has

the same swirl direction throughout.

In actual fact, the axial reverse flow, which is being sucked into the vortex core region, has no initial angular momentum. Its total momentum, although much lower in magnitude, is imparted to it by the friction of primary exhaust flow or other complex momentum exchange mechanisms undergone during turbulent flow. It can be expected, therefore, that the maximum tangential velocity gradient ($\partial V_{\phi}/\partial r$) will occur in the region where axial reverse flow starts (i.e. where $V_z = 0$). It is precisely in this region that the maximum transfer of tangential momentum is taking place. Experimental results confirm this finding.

From the analysis of the experimental results of the radial distributions of both axial and tangential velocity components, one can confidently conclude that the maximum shear stress occurs in, or near, the region where axial reverse flow starts. This finding has real practical significance because, in attempts to minimize the losses in practical devices utilizing strong vortex motions, it may sometimes be advisable to try to eliminate, partially or completely, the reverse flow phenomenon. For example, a solid cylinder, with a circular area approximating that of the reverse flow area, may be incorporated into the core

region of a vortex chamber. A patent on a fluidic vortex rate sensor has been obtained by Kwok [16] who employed exactly this technique when he introduced a cone-like solid body along the axis of his vortex rate sensor. The patent claims that both the sensitivity and stability of the rate sensor are substantially imporved. The results of our investigation support the validity of this claim.

4.1.3. Radial Distribution of Radial Velocity Component

Before discussing the radial distributions of the velocity component which were obtained under the test conditions shown in Figs. 8 and 9, the sign convention must first be clarified. The radial flow moving inward towards the centre is considered positive.

As the vortex flow exits through the central exhaust port, which consists of a tube 2 inches in diameter by 3 inches long, as shown pictorially in Fig. 3, it resembles flow along concave walls. The destabilizing effects of centrifugal forces create stationary Taylor-Görtler vortices along the inner walls of the exhaust port. These vortices, rotating about the axis which corresponds to the spiral path of the main flow, form a vortex ring. This vortex ring is not, in fact, really a closed ring in the

conventional sense. It may be imagined that the main exit flow path resembles the wire coils of a spring. The Taylor-Görtler vortices, rotating about the flow path, are super-imposed on the main spiral outward flow. The "first" row of the Taylor-Görtler vortex ring is bounded by the wall and by the first point where V_r equals zero. Since the region immediately surrounding the exhaust hole was not measured, the limited data presented do not clearly indi-cate such a flow configuration.

Due to the rotation of the "first" row of Taylor-Görtler vortices, another similar "second" vortex ring is induced. The "second" vortex ring is shown to occur in the region bounded by the first and second points (counting from the edge towards the centre) where the radial velocity is zero. This induced "second" vortex ring is rotating in the opposite direction to the "first" but also follows the spiral outward path of the main flow.

The most significant discovery from the experi-mental data is that the radial velocity distributions reveal the existence of complex Taylor-Görtler vortices. According to the flow described above, the resultant radial velocity distribution must approach that of a sine wave. In order to clearly understand this phenomenon, it may be instructive

to consider the projected linear velocity of a point moving around a circular path as in simple harmonic motion. The magnitude of the velocity of the point when it is projected onto the plane perpendicular to the path must necessarily resemble that of a sine wave. In the present case, the flow may be visualized using this highly simplified model, although the actual flow is more complex due to the super-position of a main spiral outward flow. Nevertheless, the results in Fig. 10 clearly indicate such a trend and sub-stantiate the interpretation of the flow model.

The "second" Taylor-Görtler vortices induce a "third" vortex ring bounded between the second and third points where the radial velocity equals zero. The rotation of the "third" Taylor-Görtler vortex ring is in the same direction as the "first" but opposite in direction to the "second" which actually induces the rotation. This behaviour is similar to that of a gear train where alternate gears rotate in the same direction. The direction of vortex rota-tion is indicated by either positive or negative radial velocity distribution as shown in Fig. 10.

It is also of interest to note that the outer boundary of this "third" vortex ring coincides with the point where axial reverse flow starts. Therefore, the "third" row of Taylor-Görtler vortices, rotating about an axis which

corresponds to the spiral path of the reverse flow, actually progresses in the axial direction opposite the main exhaust flow.

From the test data, it can be observed that there is yet a "fourth" row of Taylor-Görtler vortices induced by the "third" vortex ring, but rotating in the opposite direction. The "fourth" vortex ring is bounded within a right cylindrical volume whose radius equals the distance between the centre and the third point, where V_r equals zero. It can also be interpreted that the cylinder diameter is twice that of the Taylor-Görtler vortices. These vortices rotate about an axis which also corresponds to the spiral path of the reverse flow.

Similar phenomena were recognized in the Ranque-Kilsch tube but the complex vortex motions and energy separation mechanism of the tube were not clearly understood. It is anticipated that our experimental data will provide a better insight into the structure of the vortex and the interfaces between various vortices within the main swirl motion.

Similar tests were conducted on two additional sets of experiments with supply flow rates of 15 and 20 scfm.

The radial distributions of axial, tangential and radial velocity components are shown in Figs. 11 to 16. Except for the corresponding increase in magnitude of the velocity components, the basic exhaust flow configurations of the vortex motions indicate approximately the same trend. It is felt that no further explanation is necessary for these two sets of results which substantiate the complex flow model proposed in the foregoing discussion.

4.2 Experiments with Constant Control Flow Rate and Different Supply Flow Rates

The second group of results are presented in Figs. 17 to 22. These data were measured in the same manner as the experiments described earlier, except that the control flow rate was kept constant during each set of experimental runs.

4.2.1. Radial Distribution of Axial Velocity Component

For constant control flow rate, the radial distributions of the axial velocity component, shown in Fig. 17, exhibit similar trends to those described in Section 4.1.1. When supply flow increases, the magnitude of axial velocity component in the outflow (positive) direction also increases. This is due to the increase in total input flow rate which must be discharged through the annular cross-sectional area bounded between the edge of the exhaust hole and the boundary where reverse flow starts (i.e. $V_z = 0$).

With the control flow rate kept constant, it can be seen that the tangential momentum imparted to the total flow remains constant. Even with different rates of supply flow, the intensity of swirl should not vary significantly. Results, however, indicate that there is a slight tendency for the reverse flow area to decrease for increasing supply flow rates. This may be due simply to the fact that all the exhaust flow has to be discharged through the annular region, as described in the previous paragraph. There is an increase in axial velocity with increasing total flow rate, but the actual increase in the axial velocity is not as rapid as that of the total flow rate. Consequently, in order that all the flow be discharged to maintain the steady

flow condition, the annular flow area must increase. This results in the decrease of reverse flow area.

It may also be noted that the negative axial velocity component in the reverse flow region appears to be fairly constant, and independent of the increase in supply flow rate. Since flow in the reverse region is due to the low pressure generated by the increase in tangential velocity near the core, the magnitude of the reverse axial velocity component would be expected to be dependent on the tangential momentum. If the initial tangential flow is the same, the reverse axial velocity component should also remain the same. Results in Fig. 17 support this argument.

4.2.2. Radial Distribution of Tangential Velocity Component

The radial distribution of the tangential velocity component for a constant control flow rate of 30 scfm, and supply flow rates of 10 and 20 scfm, is shown in Fig. 18. The relative magnitudes of the control and supply flow rates indicate that a very strong swirl component is imparted to the main flow.

The general trend of tangential velocity dis-
tribution is very similar to that presented in Section 4.1.2.
However, there is an interesting finding related to the
difference in magnitude of the tangential velocity component.
Since the control flow rate is constant, and the tangential
momentum imparted to the total flow is therefore also
constant, it would seem logical to expect that the radial
distribution of the tangential velocity component would
be identical, even for different supply flow rates. Experi-
mental results, however, displayed a definite trend towards
the higher tangential velocity component for higher supply
flow rate with constant control flow.

From the physical point of view, it may be thought,
with considerable justification, that complete mixing of the
control and supply flows takes place before leaving the
central exhaust port and that, therefore, the tangential
momentum of the control flow is fully imparted to the total
flow. Since the frictional losses on the wall are a function
of both the velocity gradient and the viscosity of the fluid,
it may be expected, for a constant control flow rate, that
there will be a smaller loss of angular momentum for the case
of larger total flow rate.

It is also deduced that a smaller reverse axial flow

area is realized for larger total flow rate with constant

control flow. As mentioned previously, the maximum shear

stress occurs at the boundary when reverse flow starts and

the loss is dependent on the product of the maximum shear

stress and the area of the contact surfaces.. Since the

circumferential area, where maximum shear stress occurs,

is reduced for larger tangential velocity, the total loss

is expected to be correspondingly smaller. Consequently,

more tangential momentum is conserved for cases of higher

total flow rate.

Both the above-mentioned effects are additive

and contribute to the evidence for the difference in radial

distribution of the tangential velocity component as shown

in Fig. 18.

4.2.3. Radial Distribution of Radial Velocity Component

Fig. 19 shows that the magnitude of the radial

velocity component increases with increasing supply flow rate,

while the control flow rate is kept constant. This means

that the strength of the Taylor-Görtler vortices for different

test runs is different, even though the overall flow configura-

tion is similar.

As can be seen from Fig. 18, the tangential velocity component is higher for larger total flow rate. With a higher tangential velocity entering the exhaust port in a flow condition resembling that of the flow along concave walls, the magnitude of $(Re\sqrt{\Theta/R})$, which governs the intensity of the Taylor-Görtler vortices, also increases. Since both the Reynolds Number and momentum thickness Θ are direct functions of the tangential velocity component, the intensity of the Taylor-Görtler vortices is therefore greater for larger flow rates. Consequently, the magnitude of the radial velocity also changes with the vortex strength.

It is interesting to note that the strength of the "fourth" row of the Taylor-Görtler vortex ring (i.e. the one closest to the centre) appears to diminish much more rapidly for cases with larger total flow rate. The same phenomenon is evident in Fig. 22 where there are identical flow conditions but a slightly reduced control flow rate. However, with the limited test data, especially near the centre of the chamber axis, it is rather difficult to draw a definite conclusion. Moreover, the magnitude of the radial velocity component is extremely small and it is suspected that the insertion of the measuring probe into the critical region

near the chamber axis might have created sufficient distur-
bance to affect the original flow pattern.

Similar test results with a constant control flow
rate of 20 scfm are presented in Figs. 20, 21 and 22. In
general, an identical trend of the flow configuration is
indicated and no further discussion is necessary.

4.3 Radial Distribution of Wall Static Pressure

Wall static pressure measurements for the two
groups of experimental conditions mentioned previously are
shown in Figs. 23 to 26. These pressure readings represent
pressures in the annular region before flow enters the
central exhaust port. The major objectives of these
measurements are to check the flow symmetry and to recognize
the general trend of wall static pressure distributions.

The radial distributions of wall static pressure
shown by the data in Figs. 23 to 26 are very similar to
those of Kwok [3] and Savino [14]. Unfortunately, the geo-
metric configuration of our test apparatus limits the wall
static pressure measurement in the exit core of the vortex.

Otherwise, an interesting comparison can be made to check
the correspondence of minimum wall static pressure readings
with the point of maximum tangential velocity. Previous
experimental results by Kwok indicated that the minimum
pressure occurs closer to the centre than to the point of
maximum velocity. However, the present experimental
investigation was not able to confirm this finding.

Figs. 23 to 25 present data for tests carried out
with constant control flow rate and different supply flow
rates. It can be seen that, with a fixed control flow rate,
higher wall static pressure corresponds to higher supply
flow rate. This is quite obvious since more pressure is
required to force the additional supply flow into the vortex
chamber.

Comparison of Figs. 23, 24 and 25 shows that the
drop in wall static pressure in the direction of flow is
more rapid for the higher control flow rate which produces
higher tangential velocity in the chamber. Since frictional
losses are a function of the velocity gradient, higher loss
would be expected to be associated with higher control flow
rates. Furthermore, as a result of the conservation of
angular momentum and the continuity equation, both the tangen-
tial and axial velocity components are expected to increase

as flow is spiralling towards the central exhaust port.
The increase in velocity is reflected in the drop of wall
static pressure.

It should be noted that the rate of decrease of
wall static pressure increases near the exhaust. As dis-
cussed above, both the tangential and radial velocity
components increase in the direction of the flow; therefore,
the drop in static pressure which is a function of the
square of the velocity vector is expected to change accor-
dingly.

Fig. 26 shows the experimental data obtained with
different control flow rates keeping the supply flow rate
fixed. From the pressure measurements, it can be observed
that the pressure increase is very high for any increment
in control flow rate. Basically, this is the principle
employed in the operation of a vortex amplifier. Briefly,
in a vortex amplifier, a small amount of control flow intro-
duced into the chamber will result in an increase in chamber
pressure such as to prevent any incoming supply flow. Even
though a higher control pressure is required to control the
supply flow, only a very low control flow rate is actually
necessary to completely cut off the supply flow which can be
many times its magnitude. The ratio of the maximum supply

flow rate to the control flow rate provides the gain of
the amplifier.

The general trend of the radial distributions of
wall static pressure is similar to those discussed. It is
hoped that these experimental data will be used for compari-
son with the theoretical curves presented by Kwok [3] and
Thinh [17] to establish the magnitude as well as the variation
of the apparent viscosity within the vortex chamber.

CHAPTER 5

CONCLUSIONS

A 10-inch vortex chamber, based on the concept of the vortex amplifier, was built for the experimental study of confined vortex motions. The chamber was designed to permit investigation of different input velocity ratios, chamber heights and exhaust orifice diameters.

Detailed measurements of the exit velocity profiles indicate the following:

(1) a strong axial reverse flow region exists in the vortex core region under high swirl conditions. The area, as well as the magnitude of the reverse axial flow, are strongly dependent on the total input tangential momentum;

(2) from the radial distribution of velocity components, the maximum shear stresses are found to occur at the edge of the exhaust hole and the boundary where reverse axial flow occurs;

(3) evidence for the existence of the Taylor-Görtler vortices is shown from the radial distribution of radial velocity components. Results indicate a total of four counter-

rotating vortex rings. Superimposed on the complex
rotation motion, there exist translation motions
with two outer vortex rings moving in an outward
direction and two inner vortex rings moving in the
opposite direction.

The experimental results of the velocity distri-
bution at the exit plane of the vortex exhaust flow provide
a better understanding of the complex flow mechanism.
Regions where maximum shear stress occur provide important
information for engineers designing practical devices utili-
zing vortex phenomena. The flow configuration may also be
useful in explaining the complexities associated with the
Rauque-Kilsch tube.

REFERENCES

1. Donaldson, C. du P. and Sullivan, R.D. Examination of the Navier-Stokes Equations for a Class of Three-Dimensional Vortices: Aero Research Associates of Princeton, AFOSR, TN 60-1277, Oct. 1960.

2. Gartshore, I.S. Recent Work in Swirling Incompressible Flow: National Research Council of Canada, Aeronautical Report LR-343, 1962.

3. Kwok, C.C.K. Vortex Flow in a Thin Cylindrical Chamber and Its Applications in Fluid Amplifier Technology, Ph.D. Thesis, McGill University, 1966.

4. Schlichting, H. Boundary Layer Theory, McGraw-Hill Book Co., New York (1960).

5. Kendall, J.N. Jr. Experimental Study of a Compressible Viscous Vortex: Jet Propulsion Laboratory, California Institute of Technology, Tech. Report No. 32-290, June 1962.

6. Kerrebrock, J.L. and Meghreblian, R.V. An Analysis of Vortex Tubes for Combined Gas-Phase Fission Heating and Separation of the Fissionable Material: ONRL-CF-47-11-3, 1957.

7. Kerrebrock, J.L. and Meghreblian, R.V. Vortex Containment for the Gaseous-Fission Rocket: J. Aerospace Science, Vol. 28, No. 9, Sept. 1961.

8. Donaldson, Coleman du P. The Magnetohydrodynamic Vortex Power Generator. Basic Principles and Practical Problems: Aeronautical Associates of Princeton, Report No. 30, Mar. 1961.

9. Williamson, G.G. and McCune, J.E. A Preliminary Study of the Structure of Turbulent Vortices: Aeronautical Research Associates of Princeton, Report No. 32, July 1961.

10. Savino, Joseph M. and Ragsdale, Robert G. Some Temperature and Pressure Measurements in Confined Vortex Fields: J. Heat Transfer (Trans. ASME), Series C, Vol. 83, No. 1, Feb. 1961.

11. Beverloo, W.A., Leniger, H.A. and Weldring, J.A.G.
    Potentialities of the Flat Vortex Hydrosifter: Brit.
    Chem. Eng. J., Vol. 8, No. 10, Oct. 1963.

12. Kendall, J.M. Jr. Experimental Study of a Compressible
    Viscous Vortex: Jet Propulsion Laboratory, California
    Institute of Technology, Tech. Report No. 32-290,
    June 1962.

13. Donaldson, C. du P. and Williamson, Guy G. An Experi-
    mental Study of Turbulence in a Driven Vortex: Aero-
    nautical Research Associates of Princeton, Report No.
    ARAP TM-64-2, July 1964.

14. Savino, J.M. Experimental Profile of Velocity Components
    and Radial Pressure Distribution in a Vortex Contained
    in a Short Cylindrical Chamber: Proceedings of Fluid
    Amplification Symposium, Vol. II, Oct. 1965.

15. Wormley, D.N. An Analytical Model for the Incompressible
    Flow in a Short Vortex Chamber: Trans. of the ASME,
    Paper No. 68-WA/FE-17, 1968.

16. Kwok, Clyde C.K. and Lapinas, Zigmas J. Angular Rate
    Sensor: Canadian Patent No. 849,793, August 25, 1970.

17. Thinh, N.D. An Analytical Investigation of Confined
    Vortex Flow Phenomena: Master's Dissertation, Sir George
    Williams University, March 1971.

Control
nozzle

Outlet

Vortex
chamber

Supply
inlet

Control
inlet
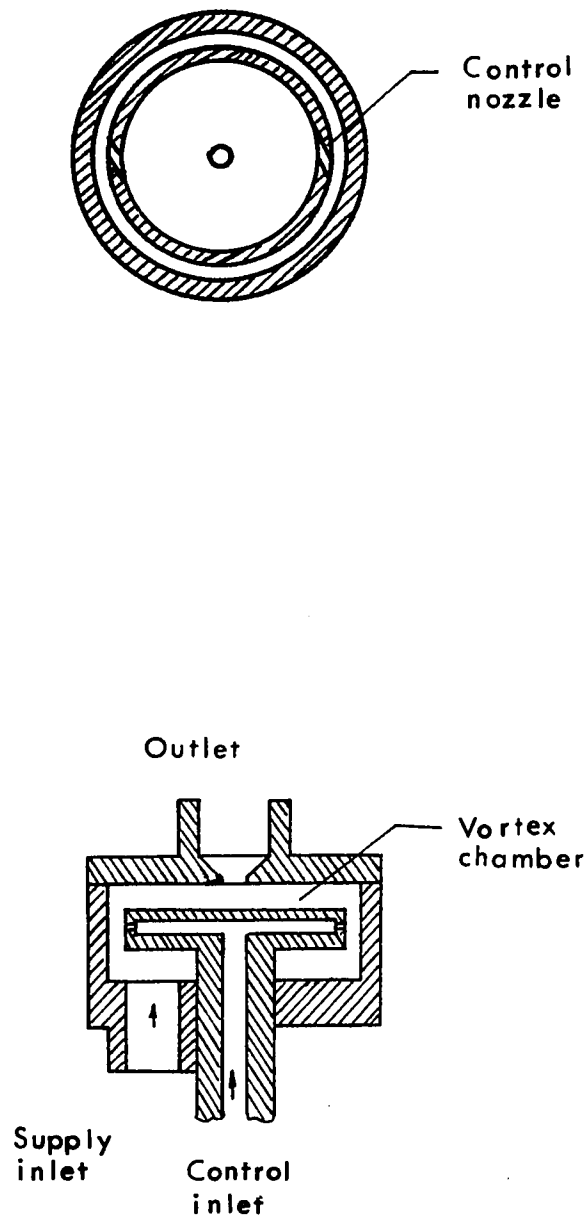
FIG. 1 Vortex amplifier schematic

FIG. 2 Experimental vortex chamber.
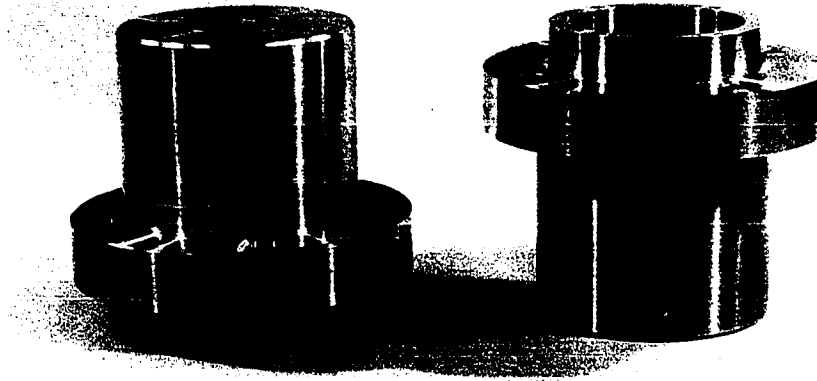
FIG. 3   Different sizes of exhaust port.
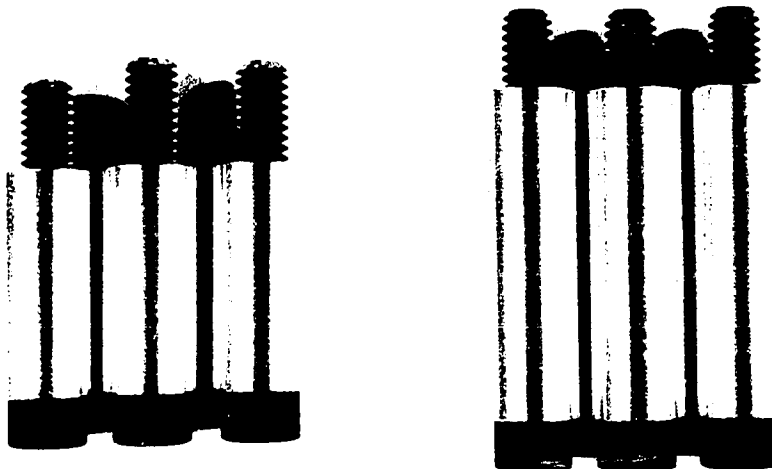
FIG. 4   Spacer for vortex chamber height adjustment.

FIG. 3 Different sizes of exhaust port.

FIG. 4 Spacer for vortex chamber height adjustment.

12"φ
10"φ
$\frac{1"}{16}$ φ Pinhole
2"φ
4"φ
3"
1"
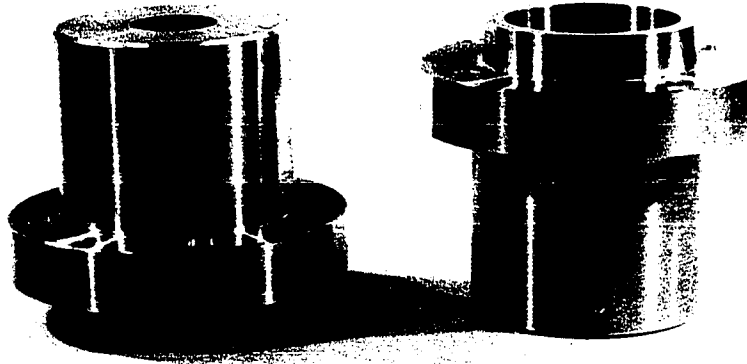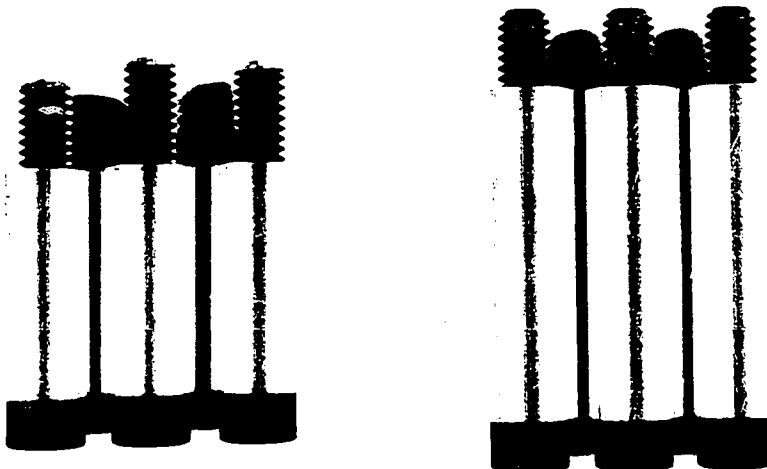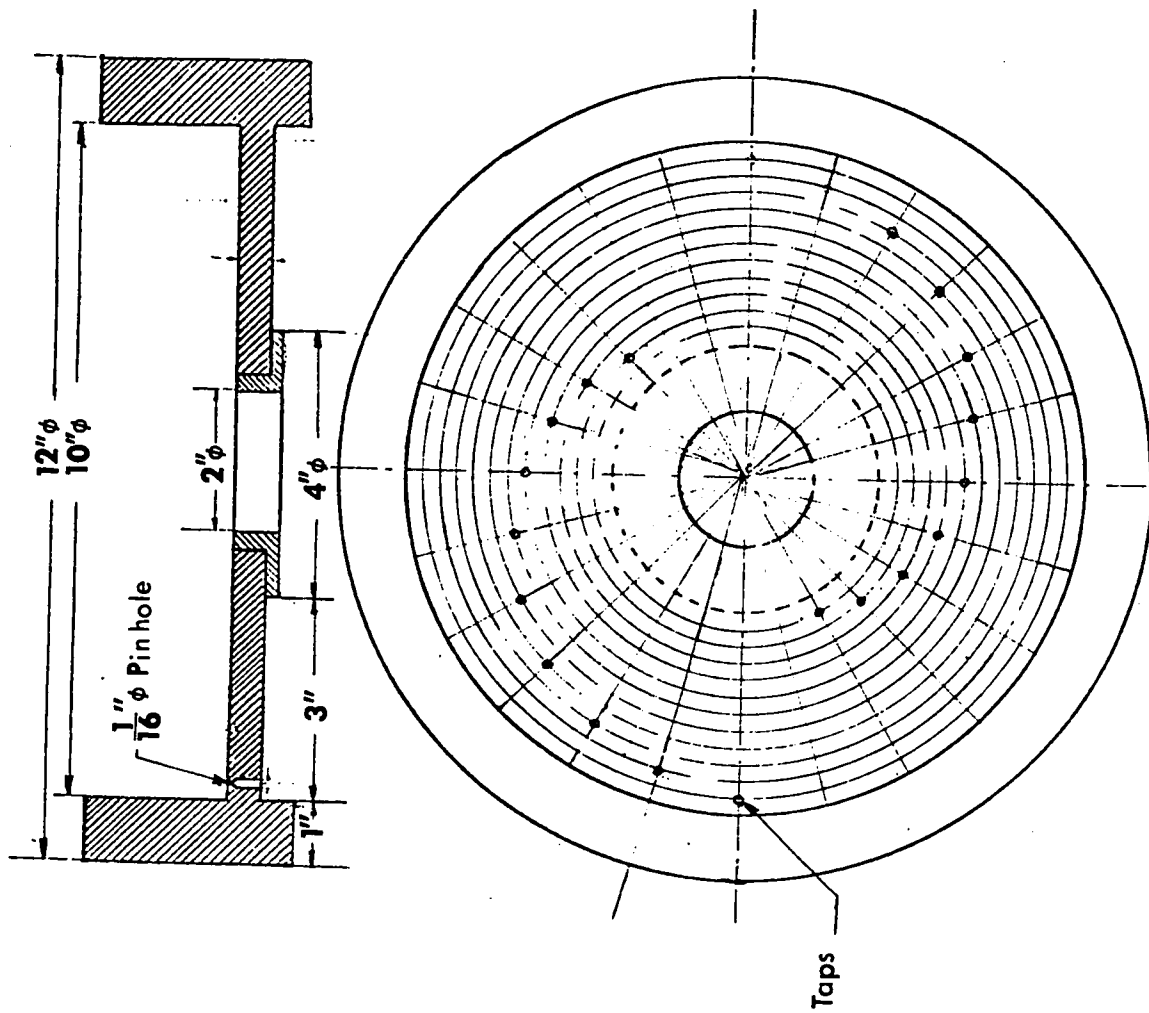
Taps

FIG. 5 Location of wall static Pressure taps.
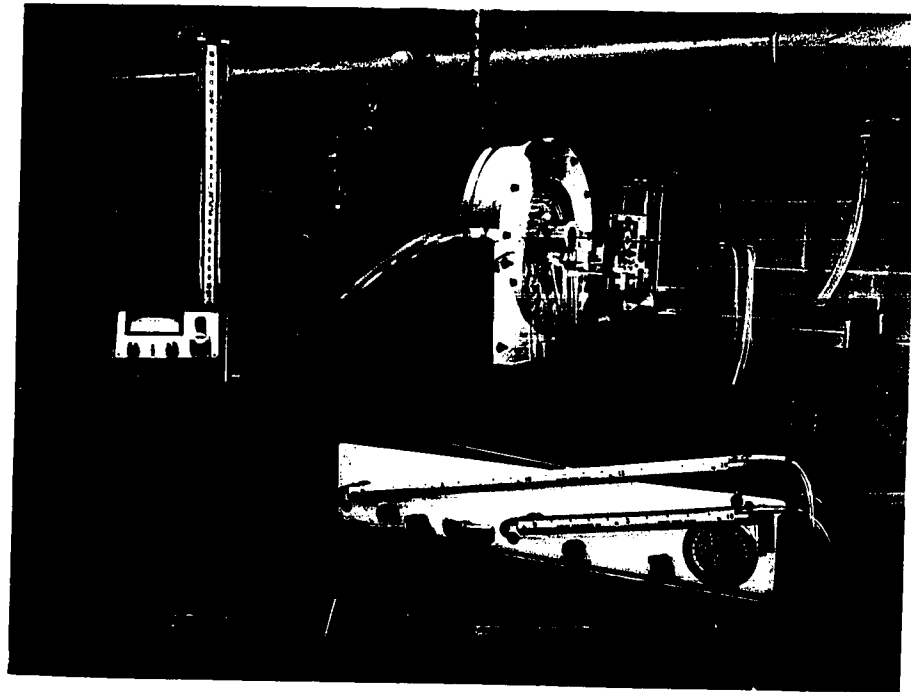
a. Overall view
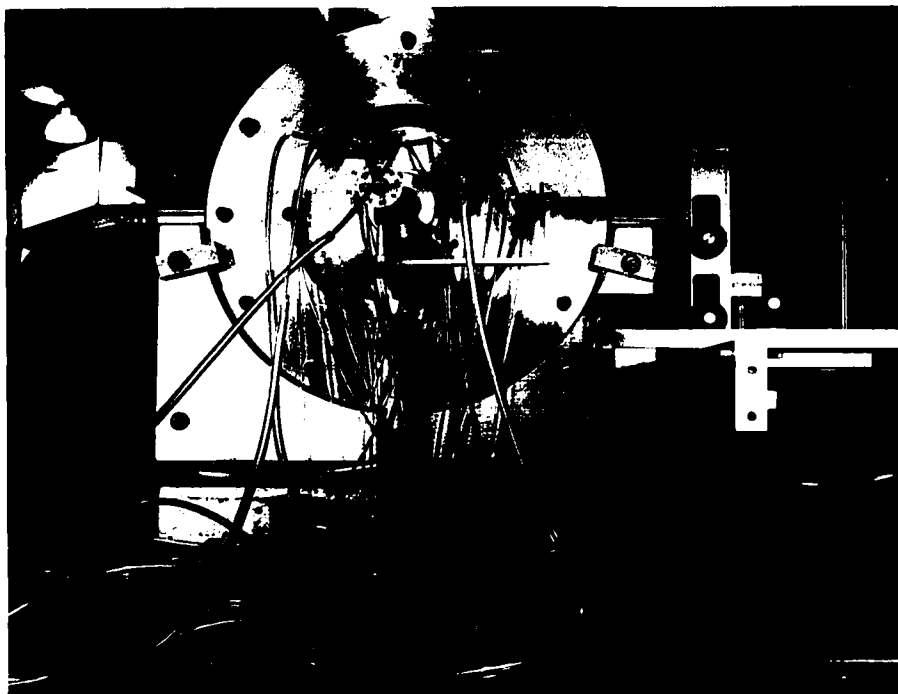
FIG. 6 Set-up
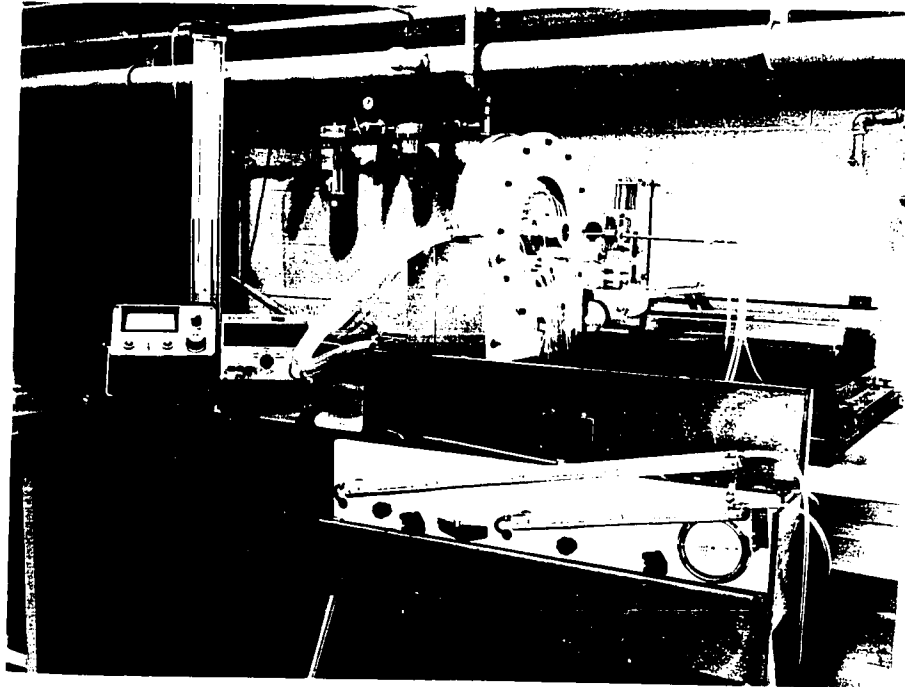
a. Overall view
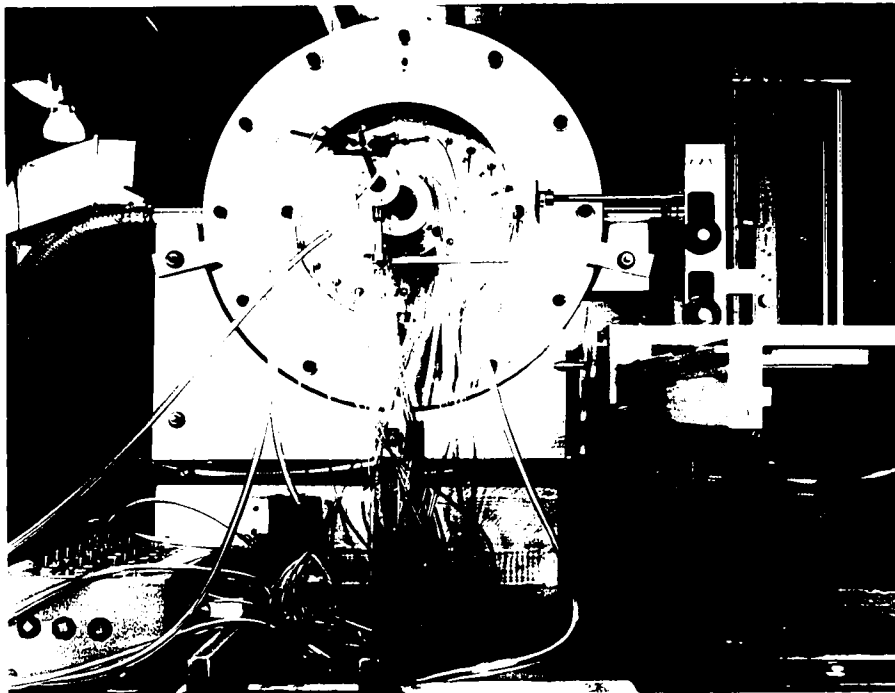
FIG. 6 Set-up
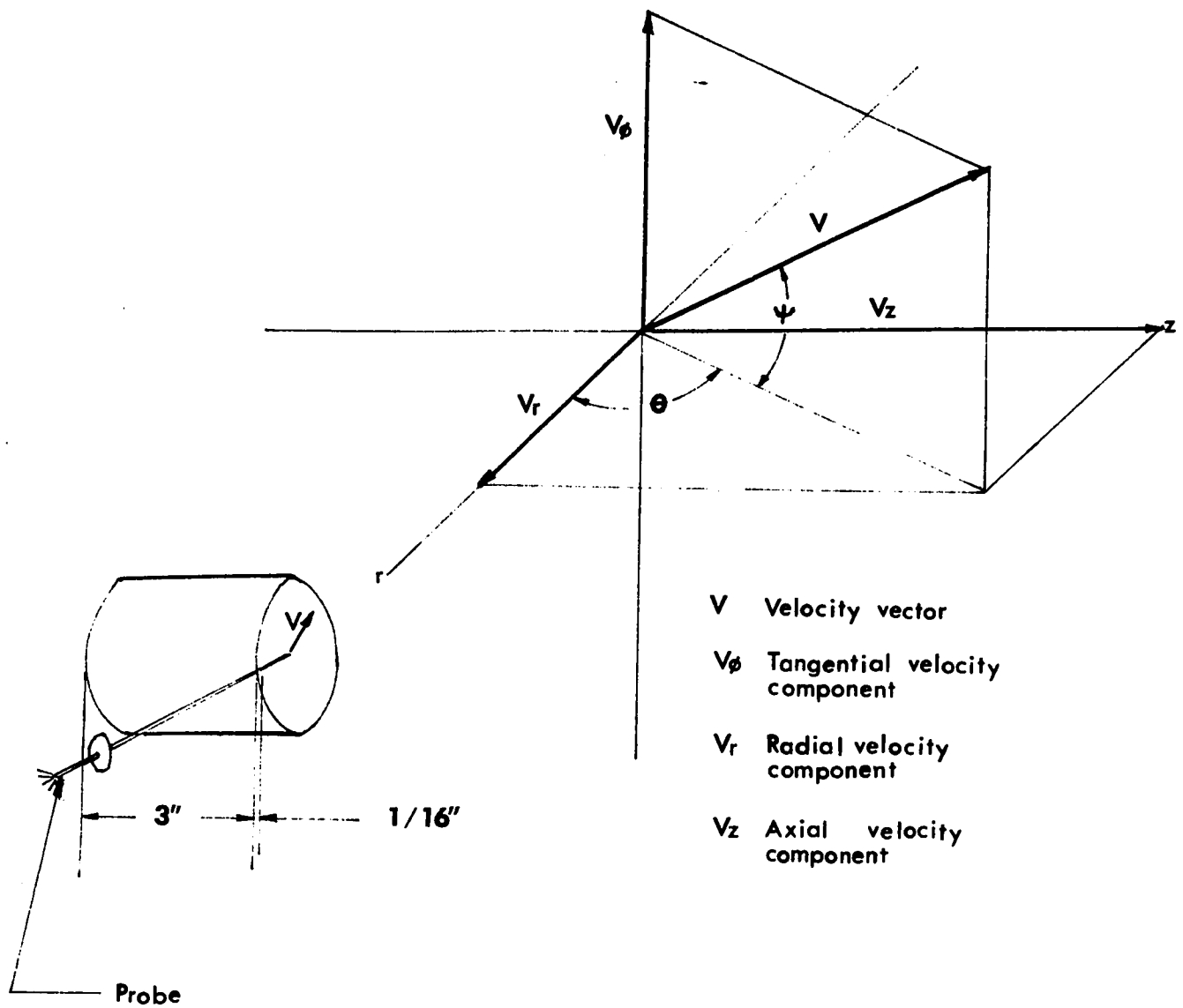
FIG. 7   Velocity   vector   and   its   components.

Supply flow rate **10** scfm.
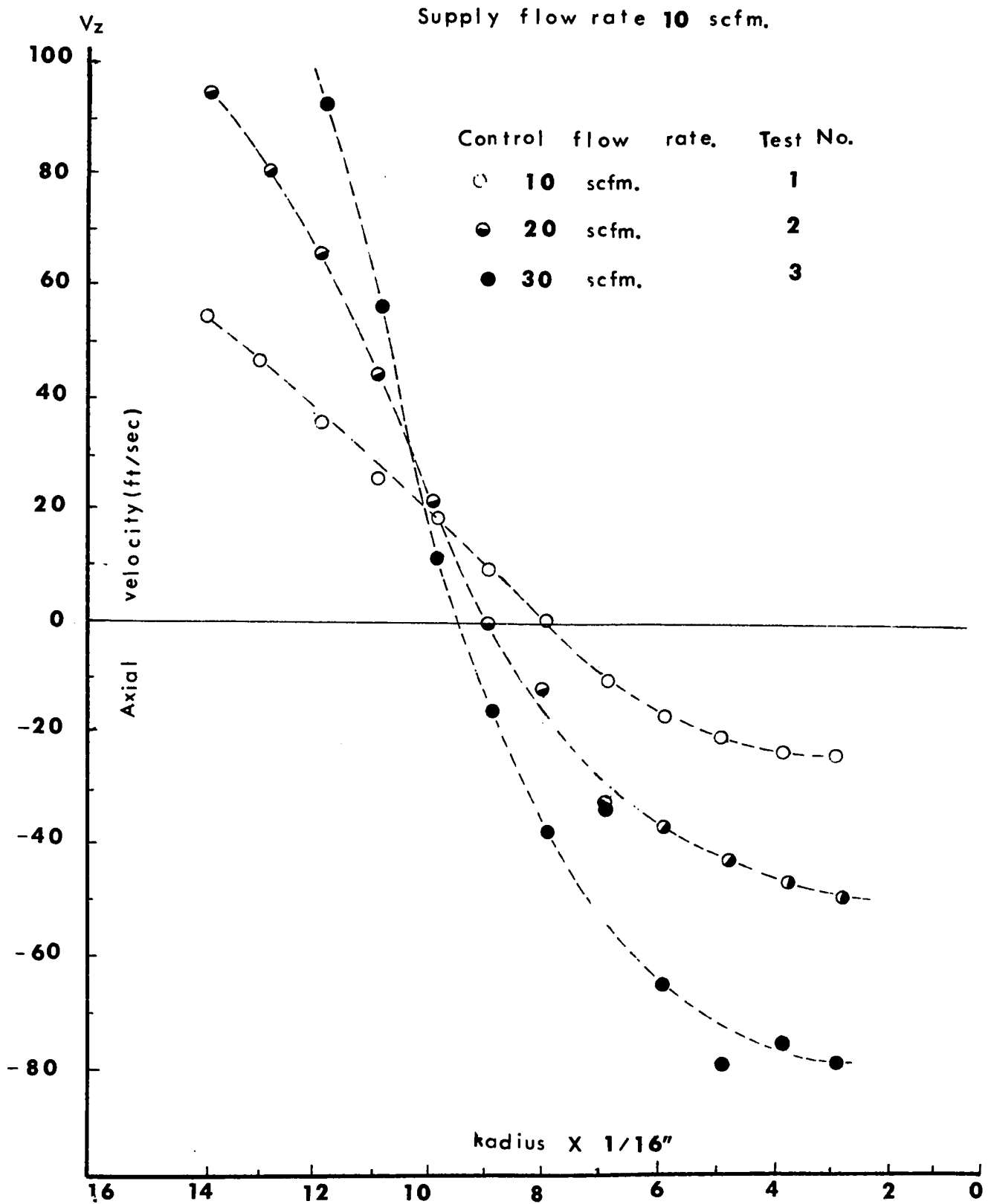
FIG. 8 Radial distribution of axial velocity component.
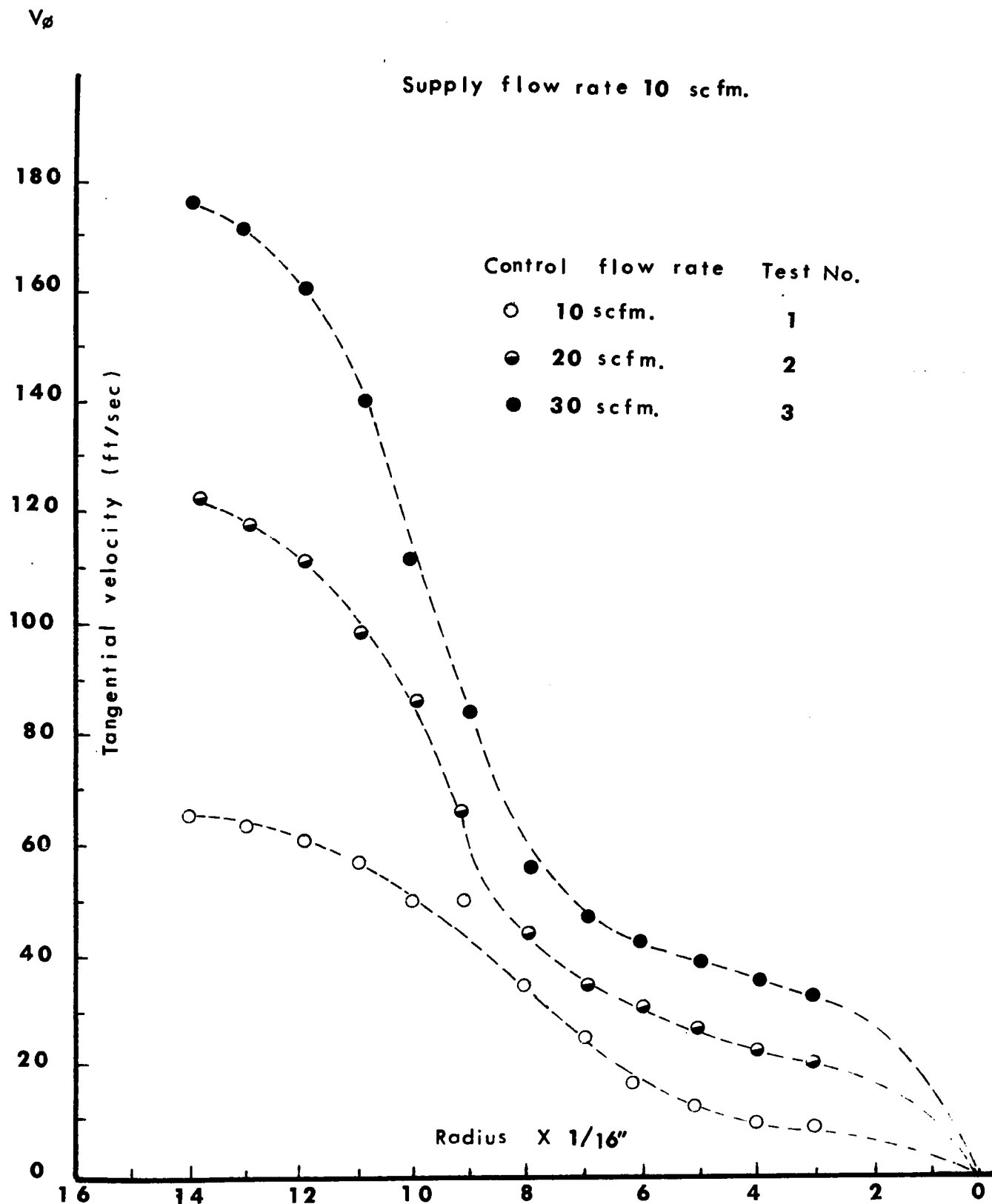
FIG. 9 Radial distribution of tangential velocity component.
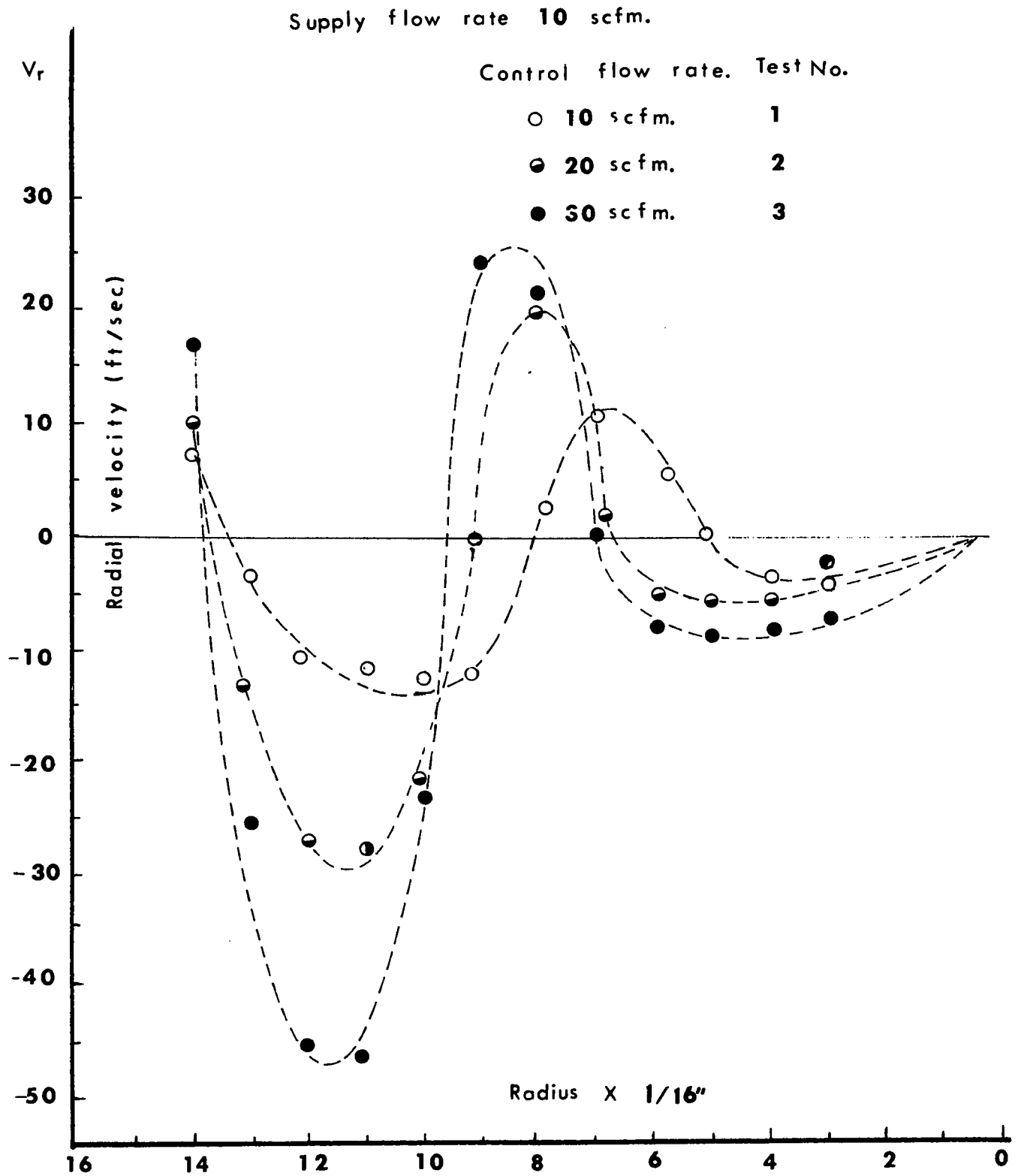
Supply flow rate 10 scfm.

V_r

Control flow rate. Test No.

○ 10 scfm.   1

◑ 20 scfm.   2

● 30 scfm.   3

Radial velocity (ft/sec)

Radius X 1/16"

FIG. 10 Radial distribution of radial velocity component.

Supply flow rate 15 scfm.

Control flow rate. Test No.
○   10   scfm.   4
⊕   15   scfm.   5
◐   20   scfm.   6

FIG. 11   Radial distribution of axial velocity component.

Supply flow rate 15 scfm.

Control flow rate.			Test No.
O	10	scfm.	4
⊕	15	scfm.	5
⊖	20	scfm.	6
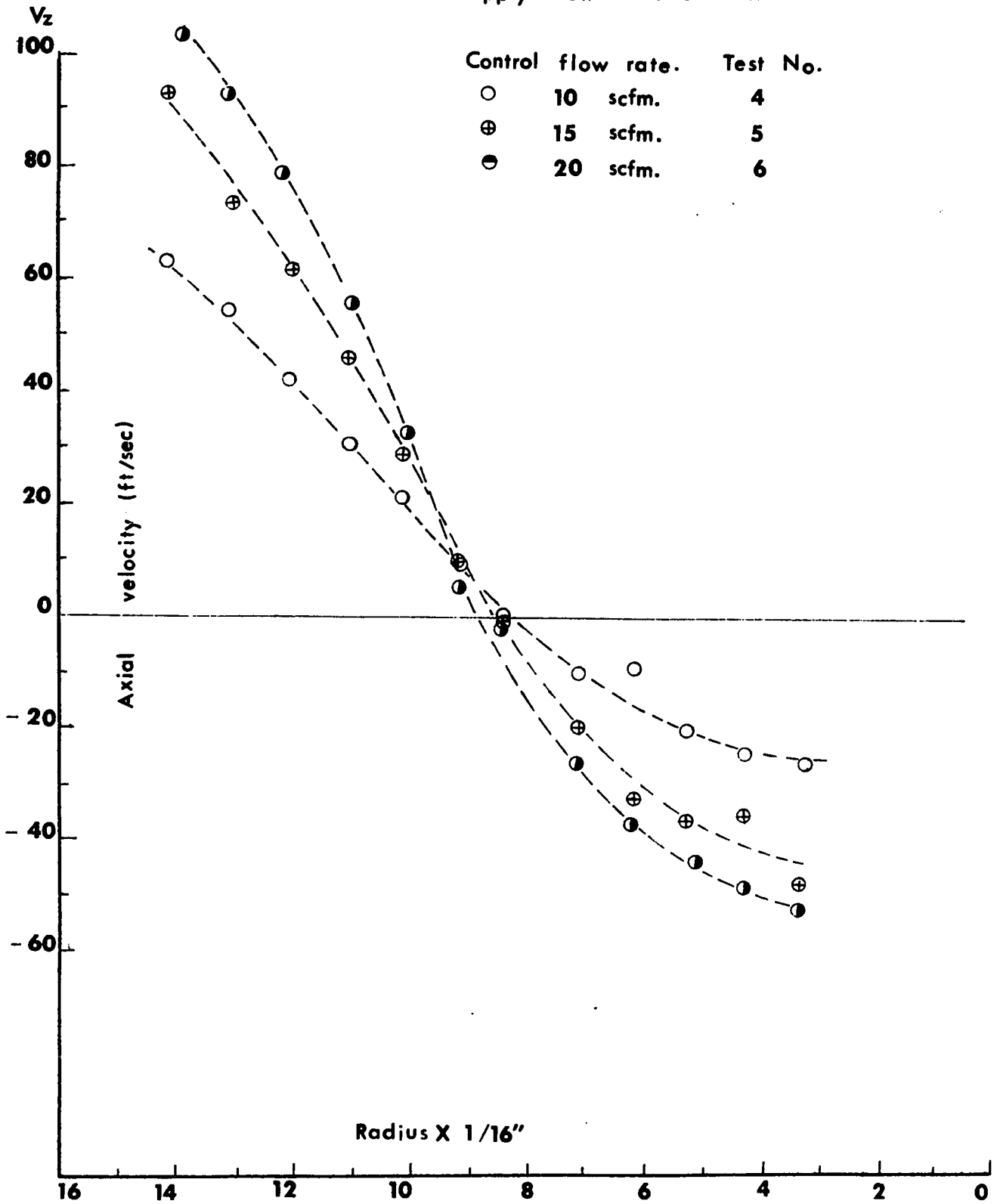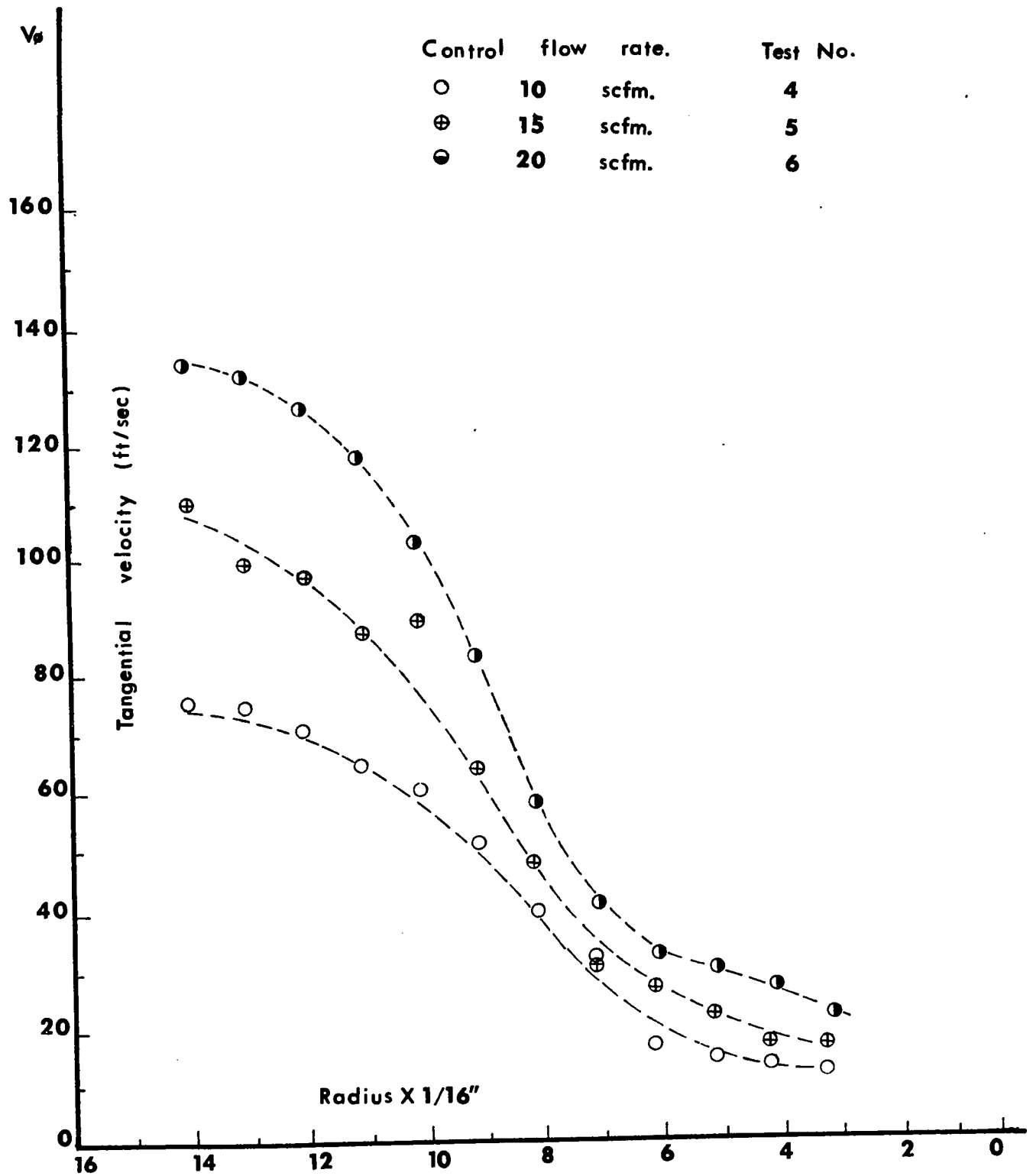
FIG. 12   Radial distribution of tangential velocity component.

Supply flow rate 15 scfm.
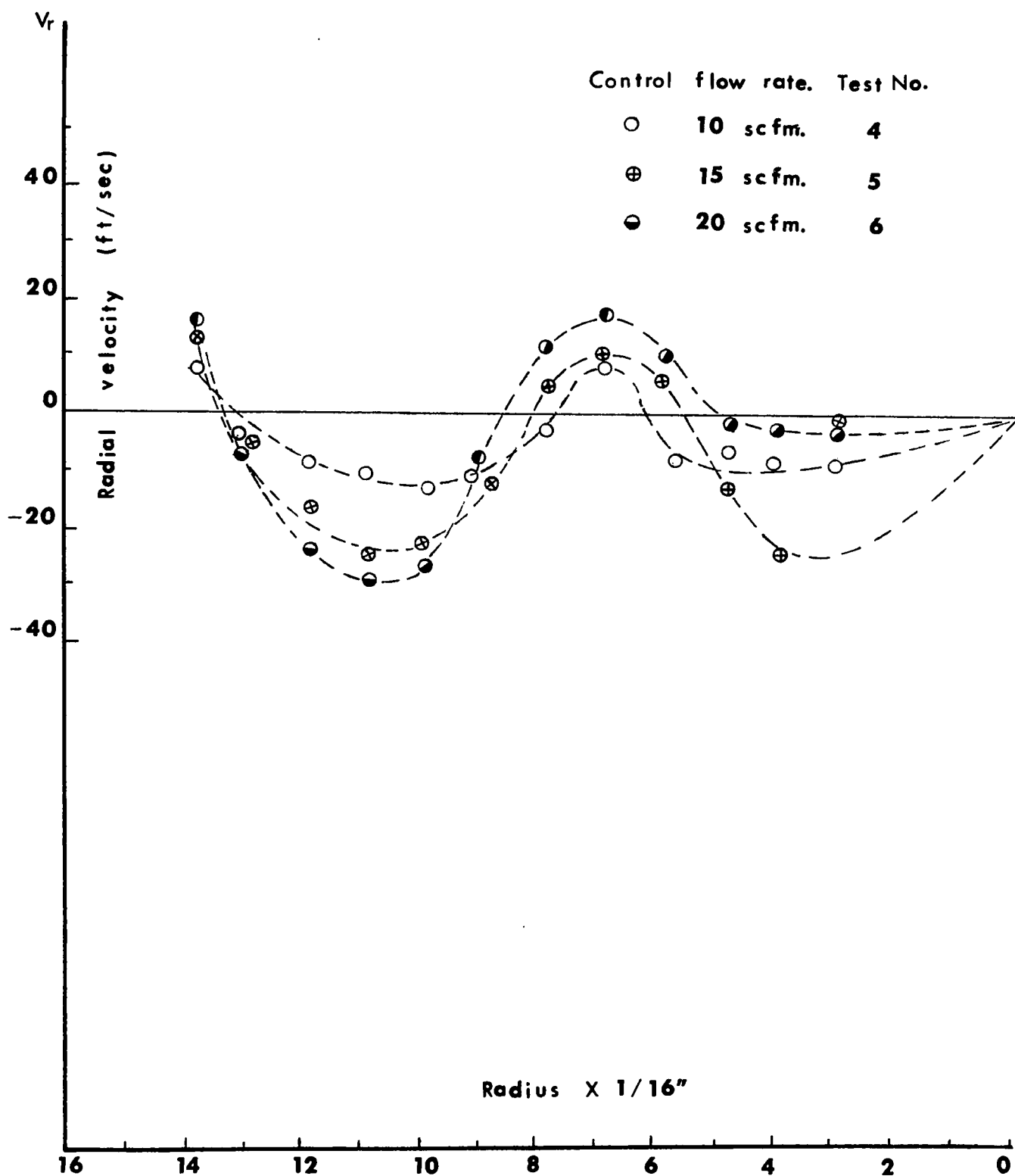
FIG. 13 Radial distribution of radial velocity.
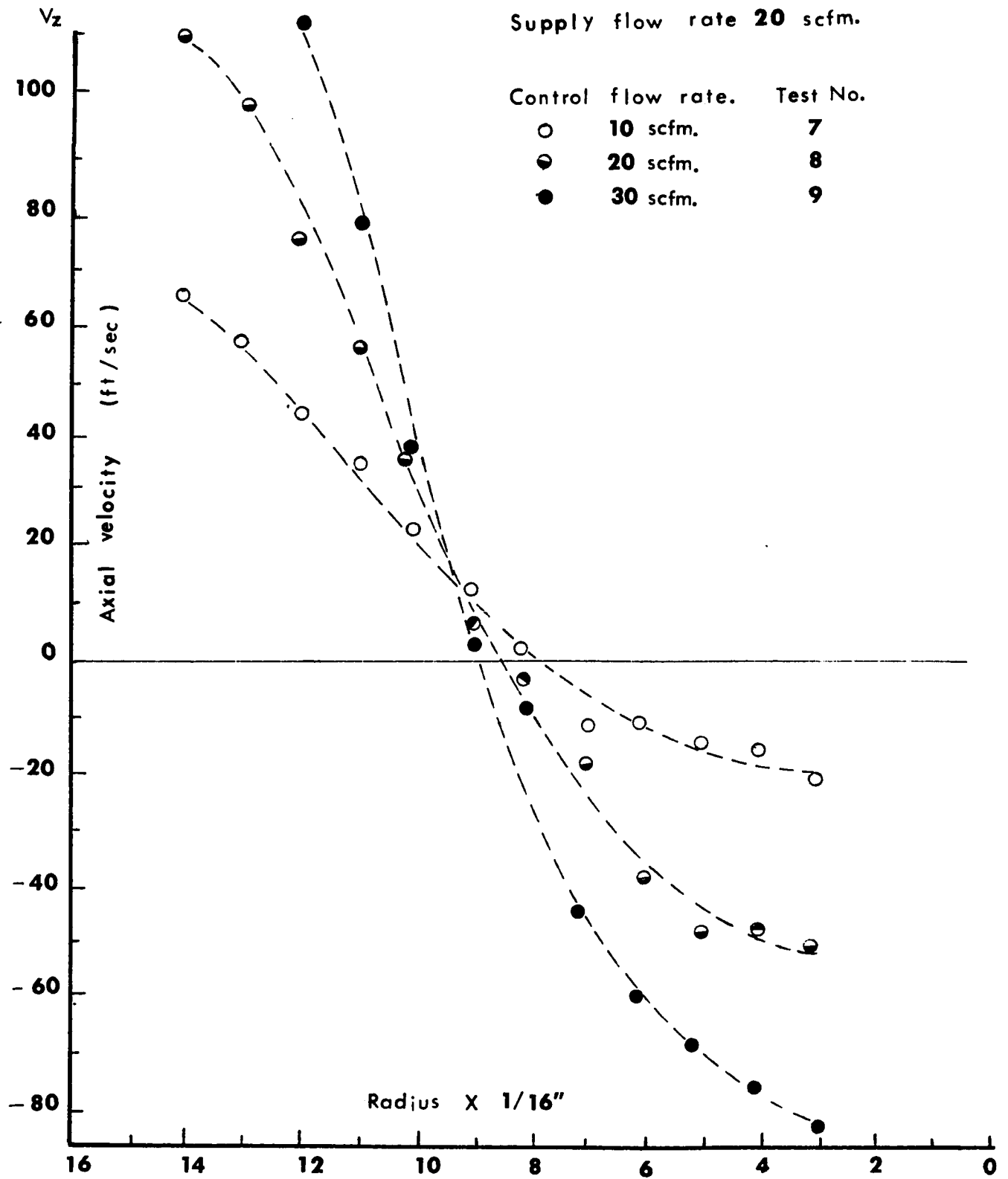
FIG. 14 Radial distribution of axial velocity component.
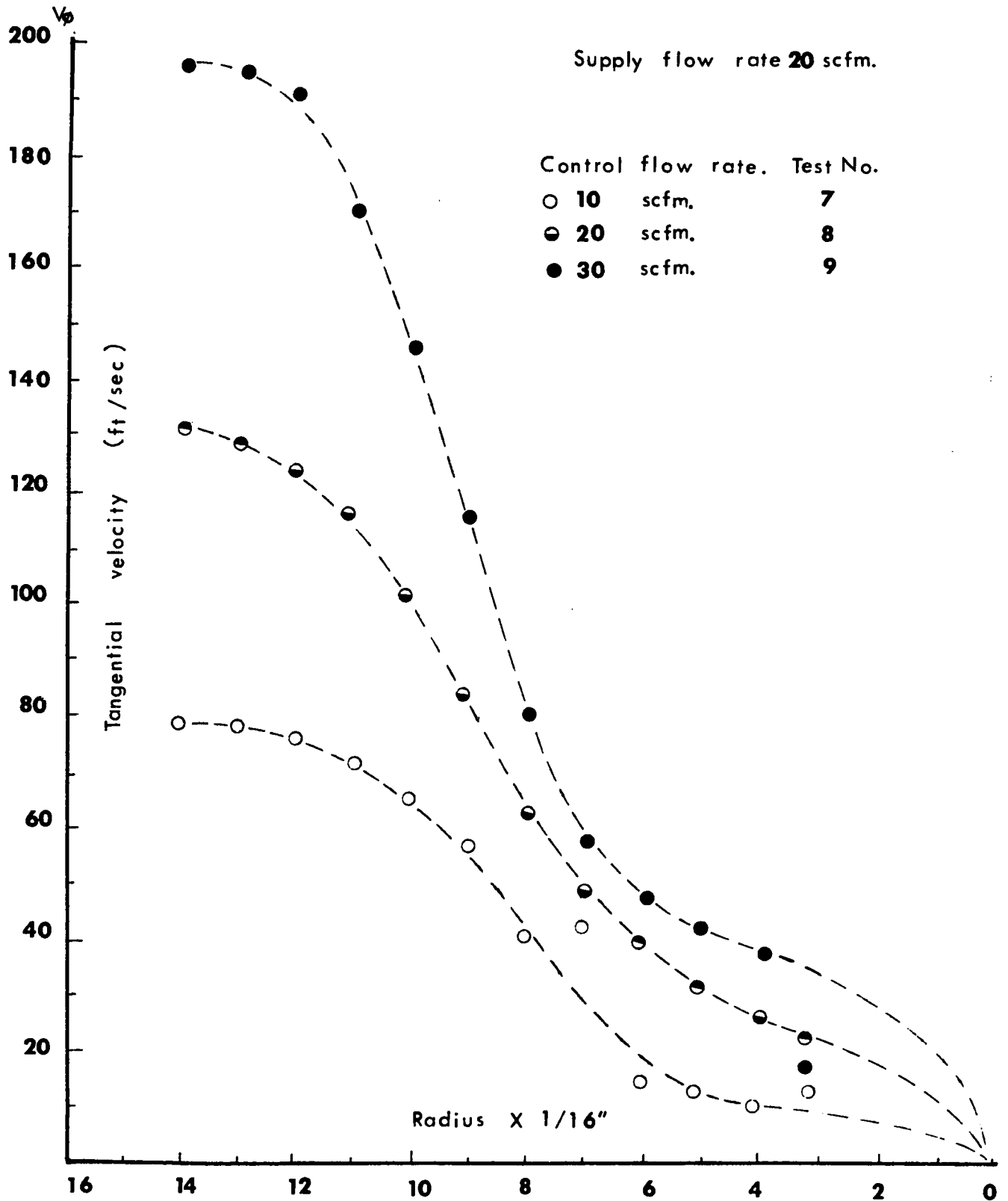
FIG. 15 Radial distribution of tangential velocity component.
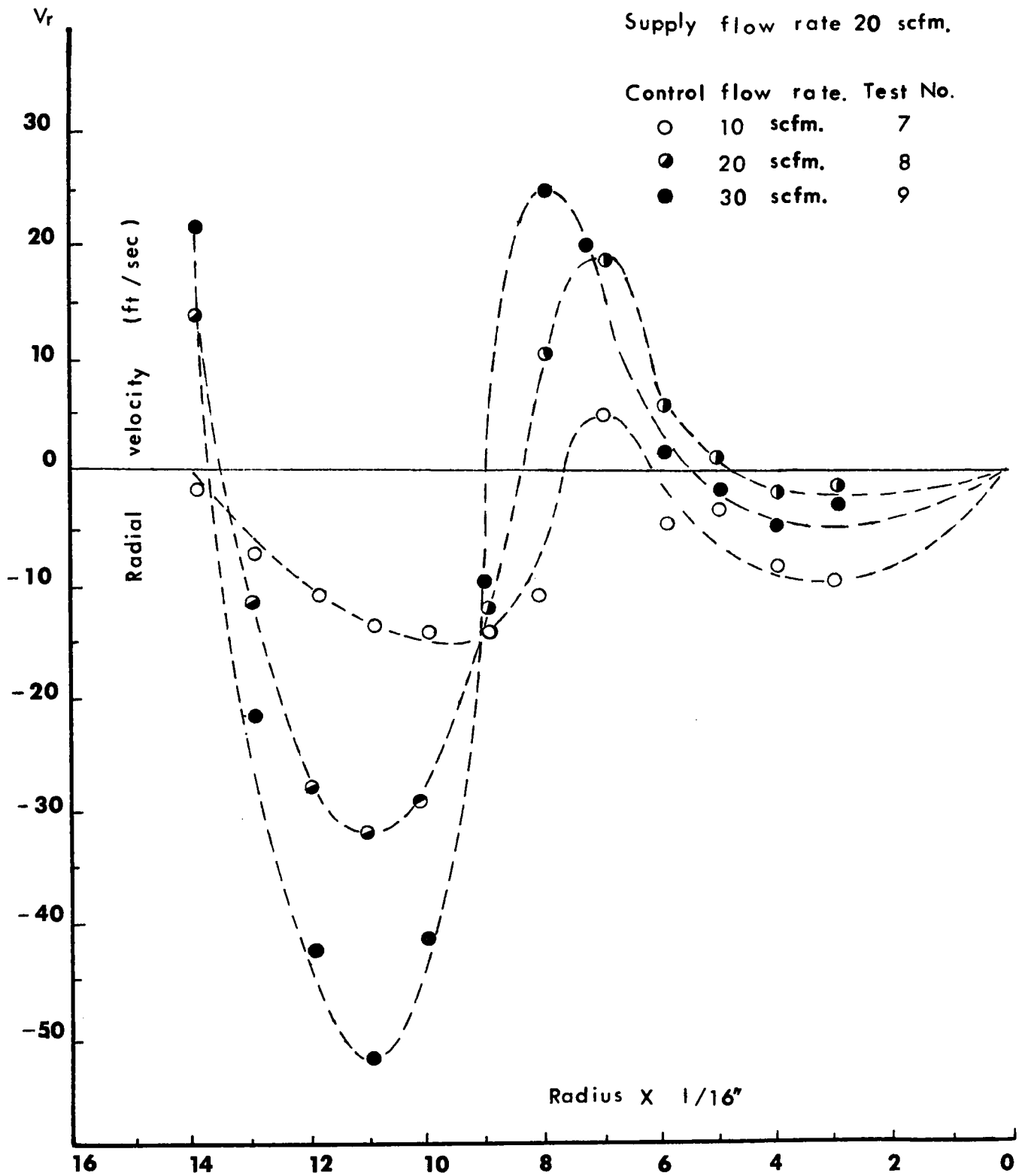
FIG. 16 Radial distribution of radial velocity component.
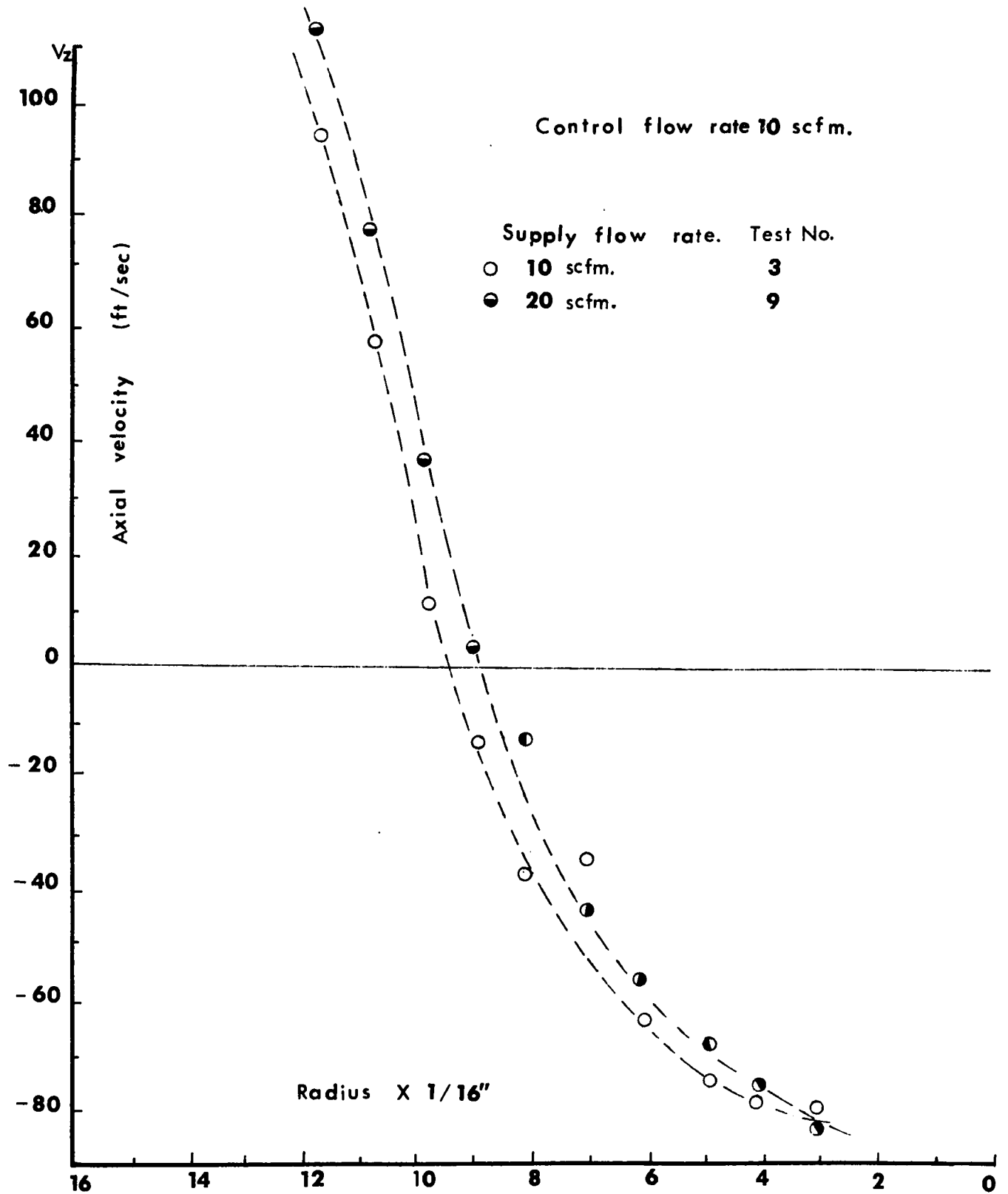
FIG. 17 Radial distribution of axial velocity component.
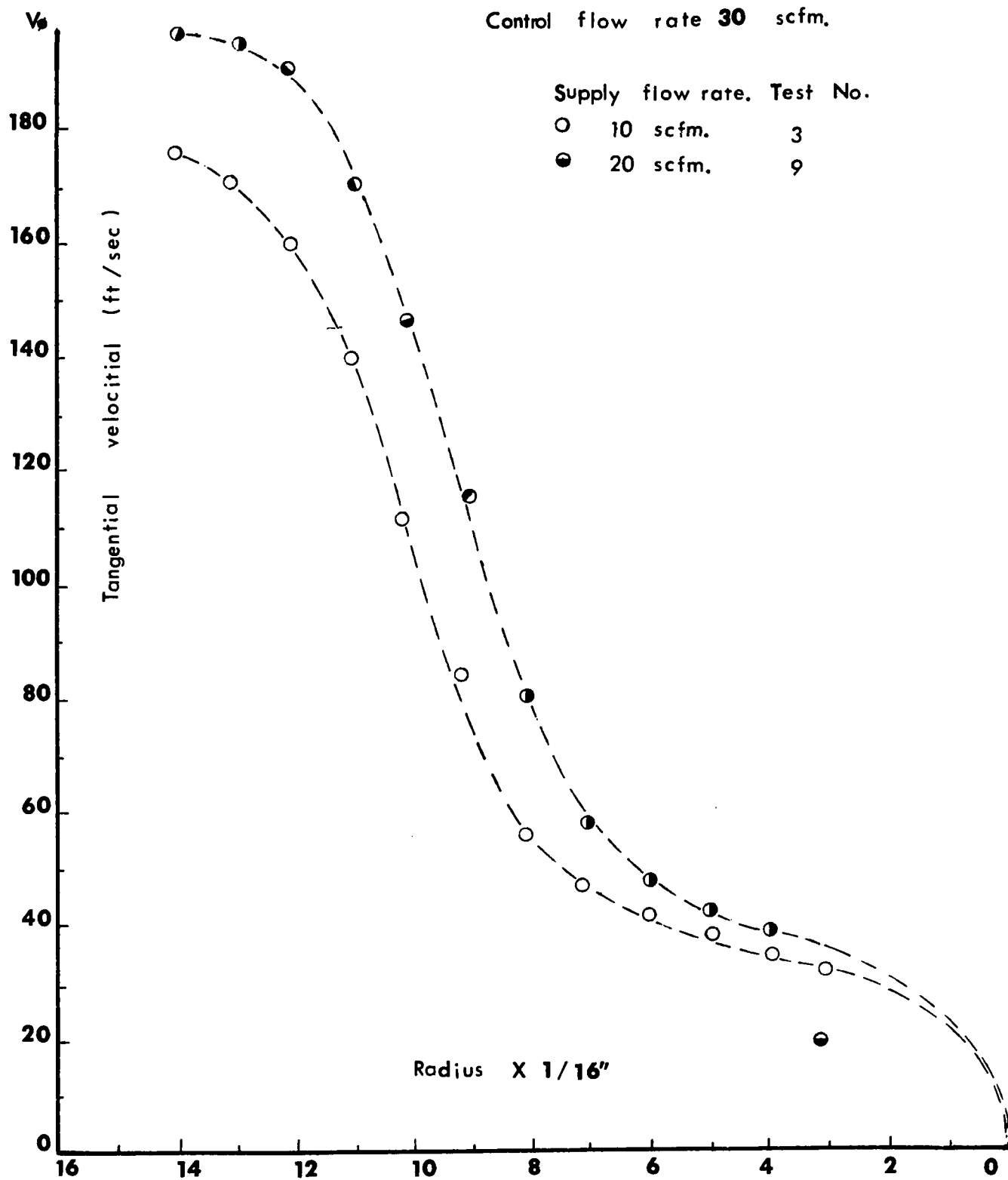
FIG. 18 Radial distribution of tangential velocity.
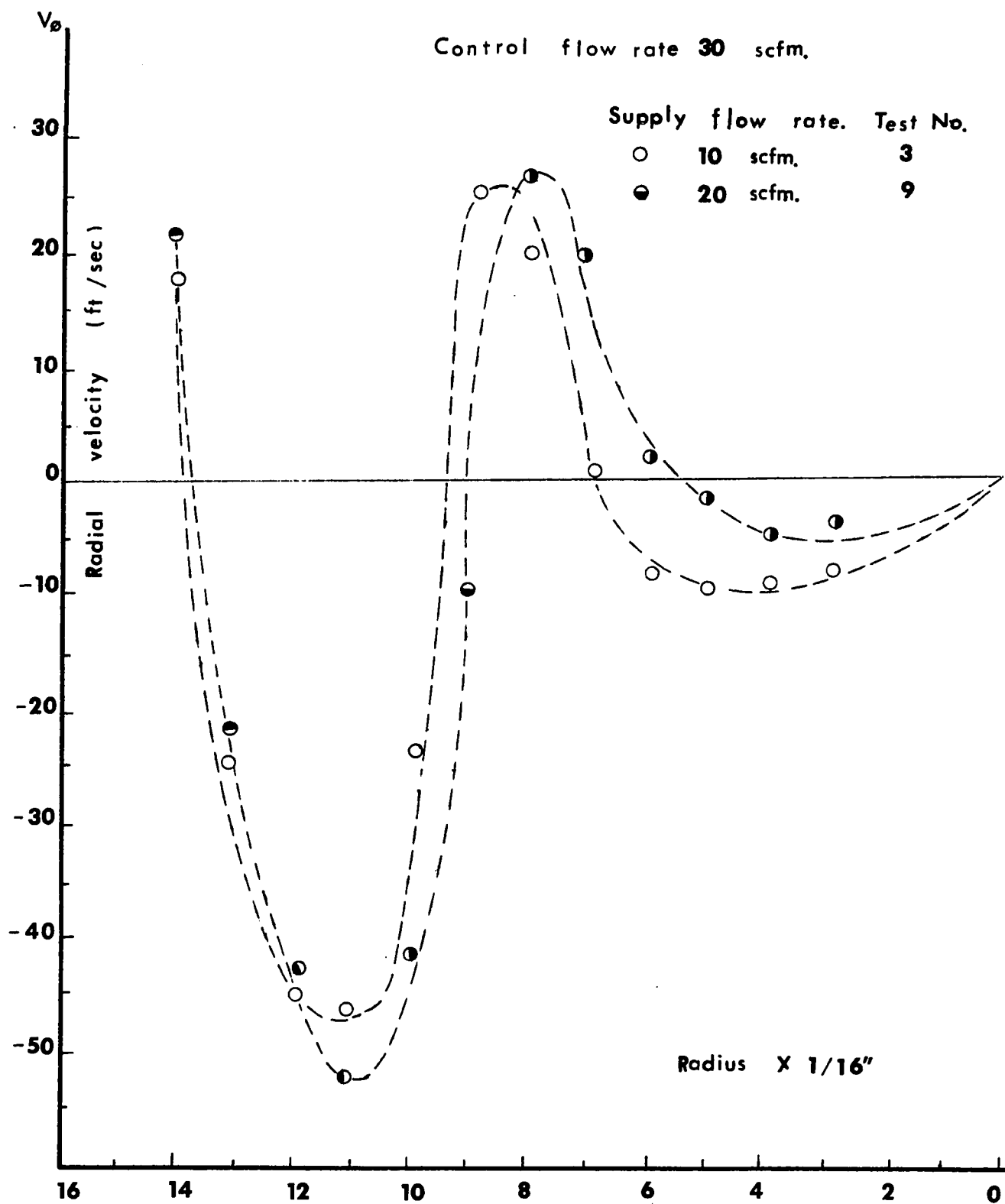
FIG. 19 Radial distribution of radial velocity component.

FIG. 20 Radial distribution of axial velocity component.

Control flow rate 20 scfm.

Supply flow rate. Test No.

○ 10 scfm. 2

⊕ 15 scfm. 6

◒ 20 scfm. 8
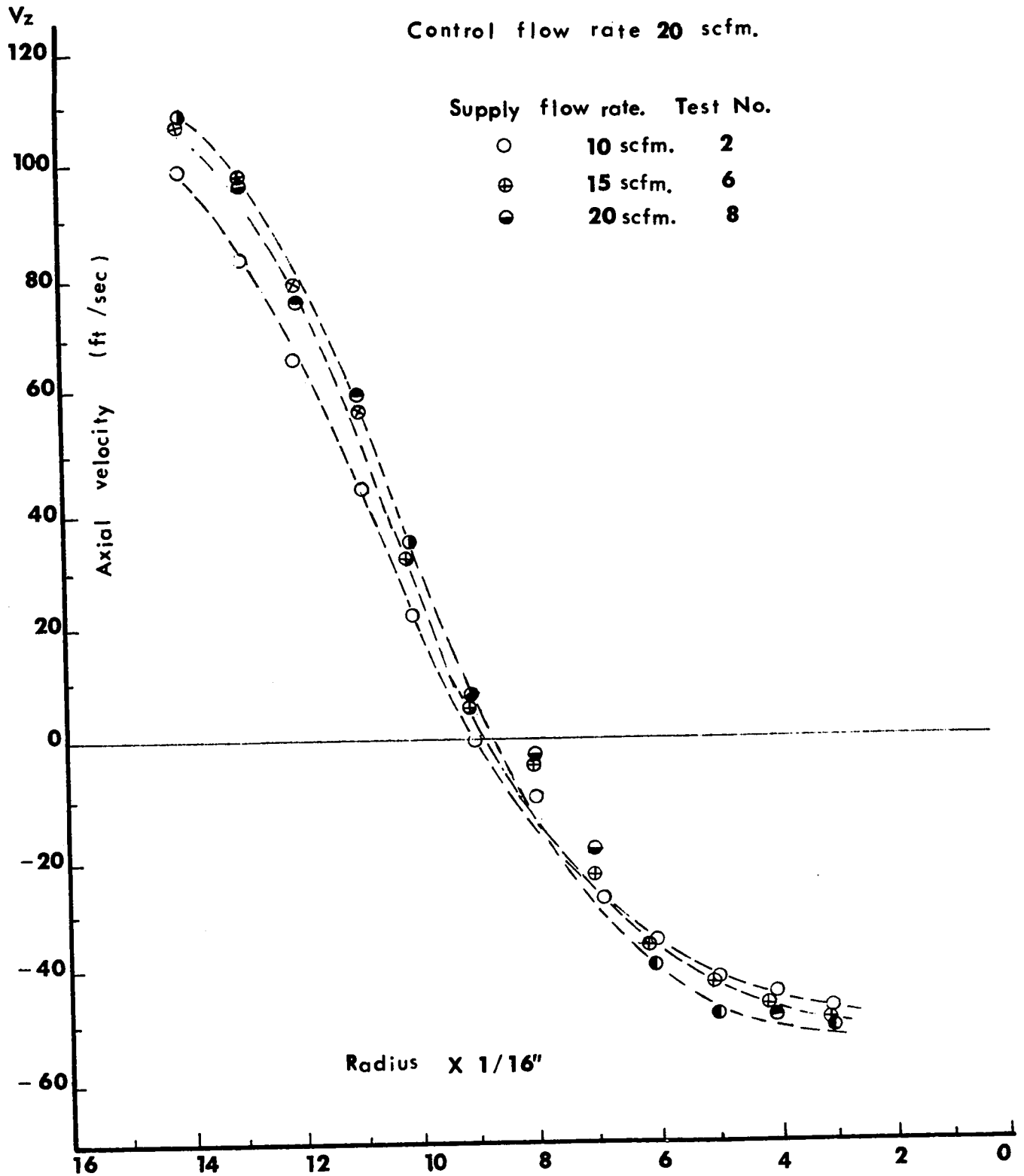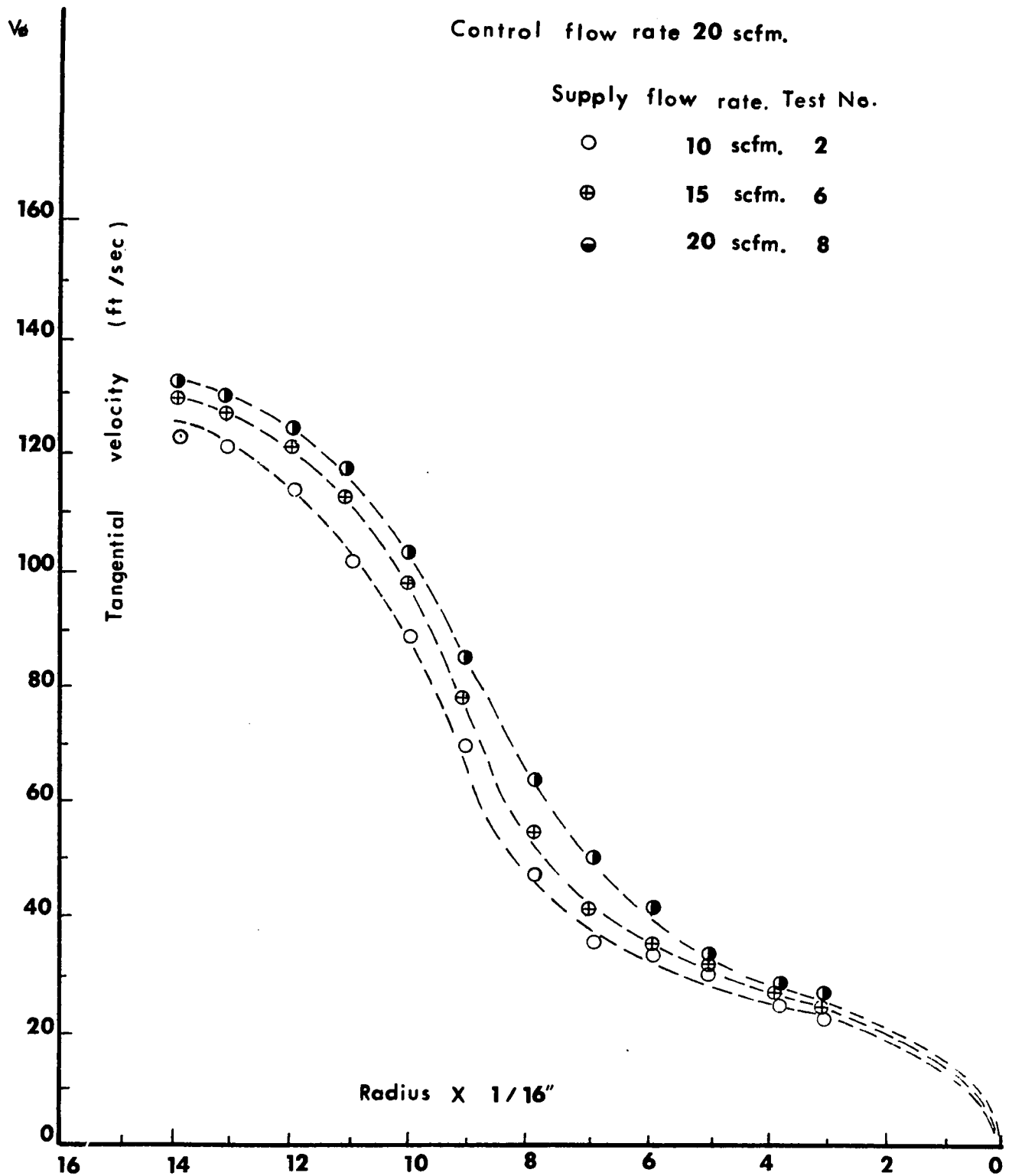
FIG. 21 Radial distribution of tangention velocity component.
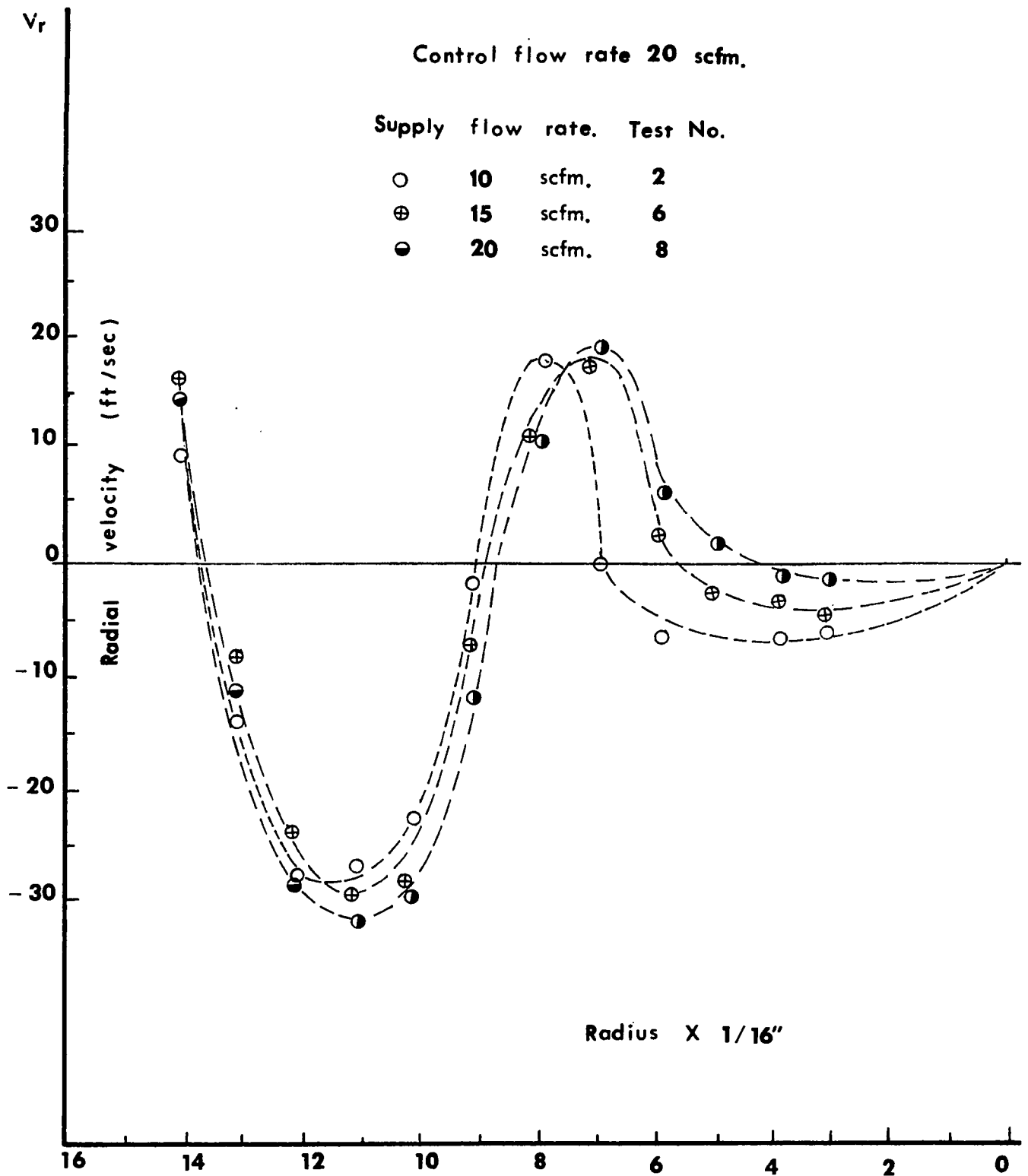
FIG. 22 Radial distribution of tangential velocity component.
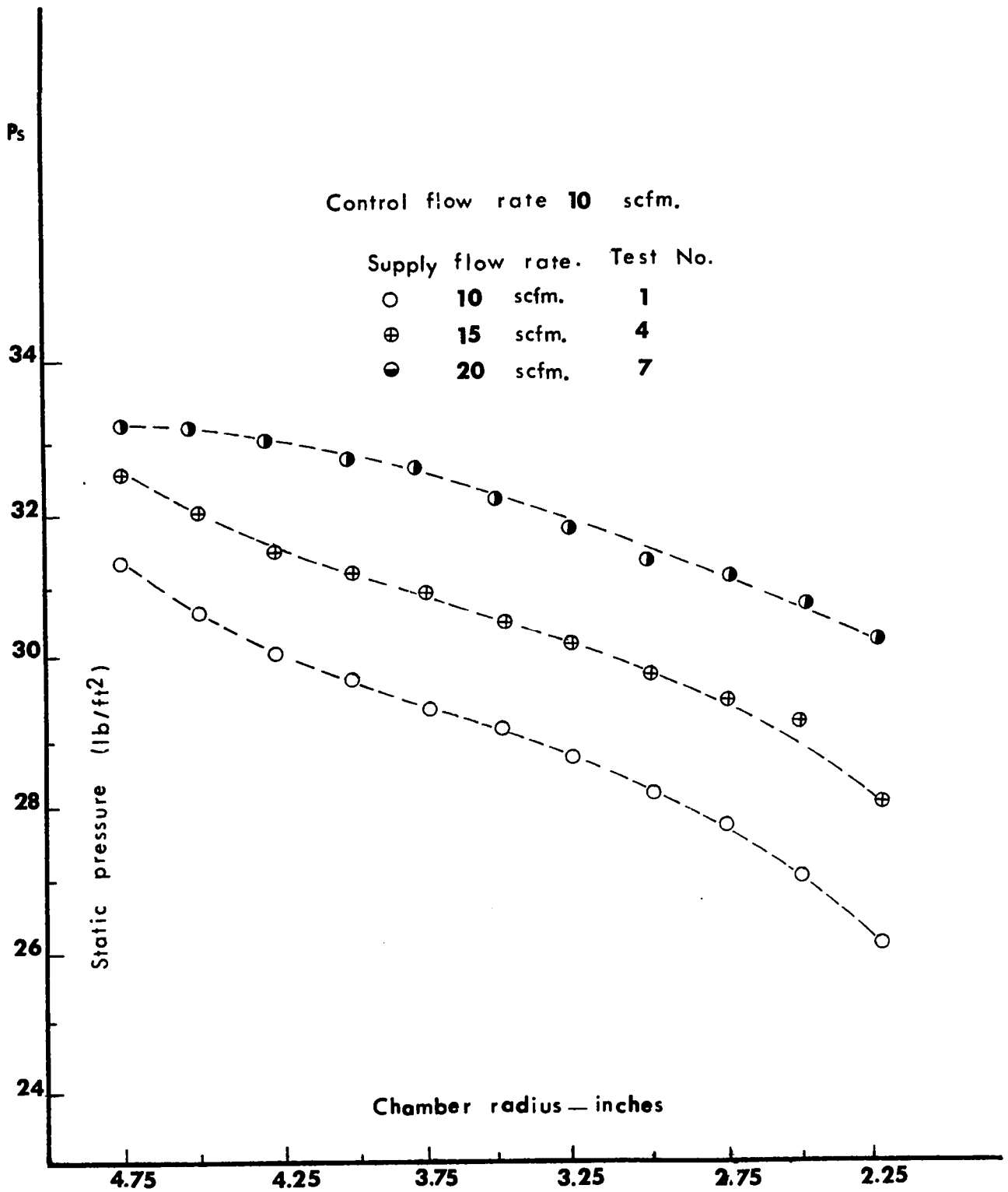
FIG. 23 Static pressure distribution in 10-in. dia. chamber.
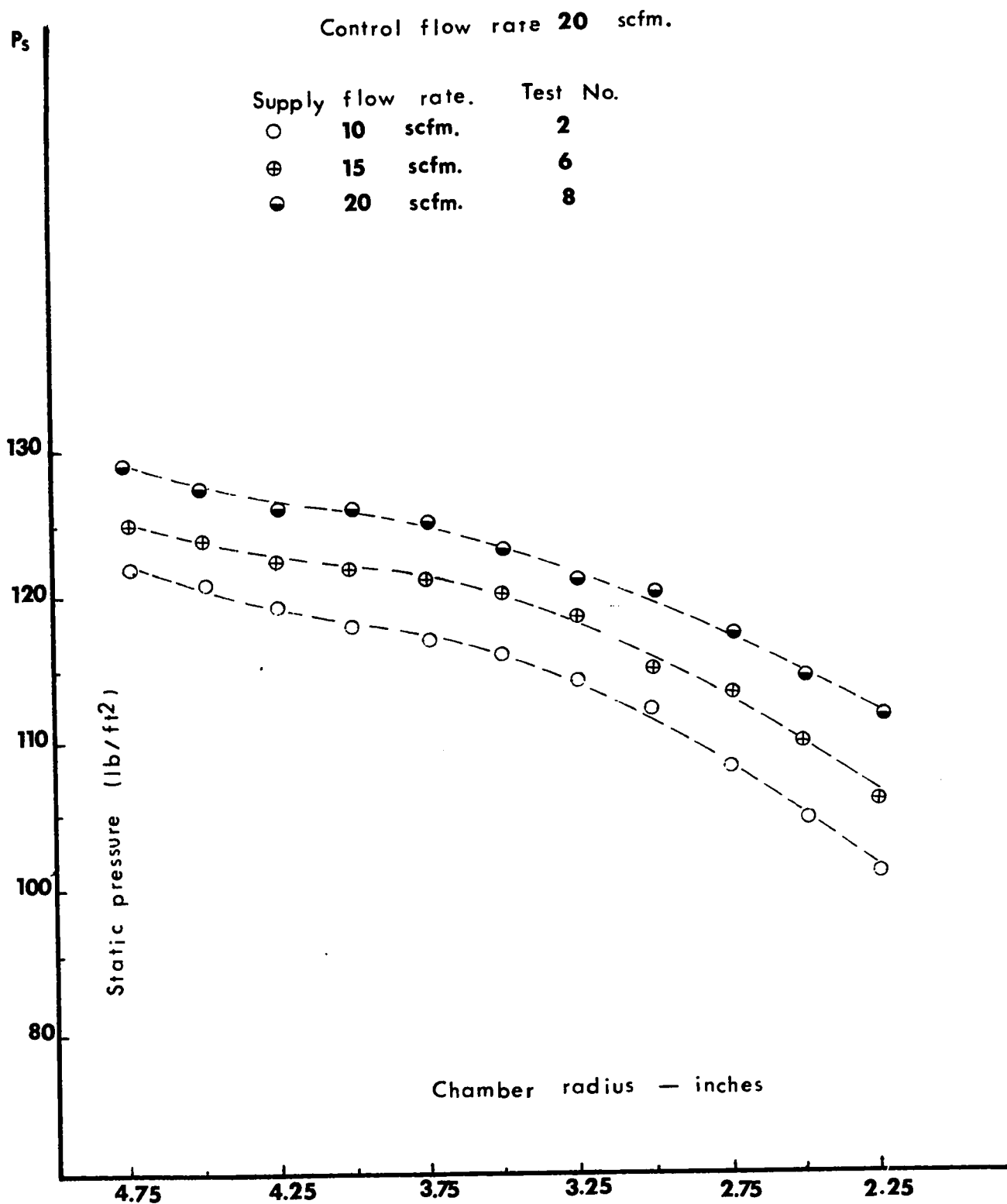
FIG. 24   Static pressure   distribution in 10-in. dia. chamber.
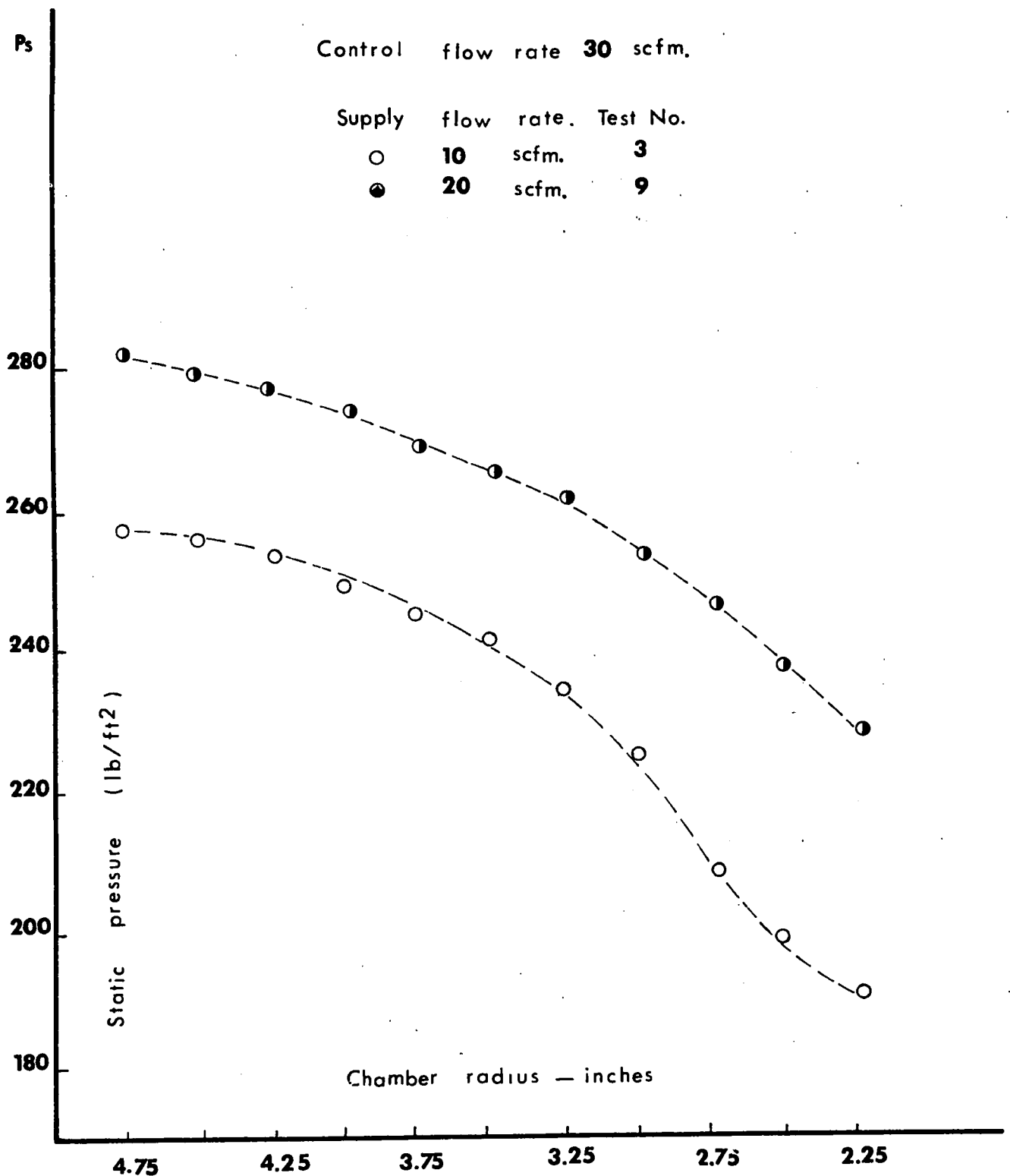
FIG. 25   Static   pressure   distribution   in   10—in   dia.   chamber.
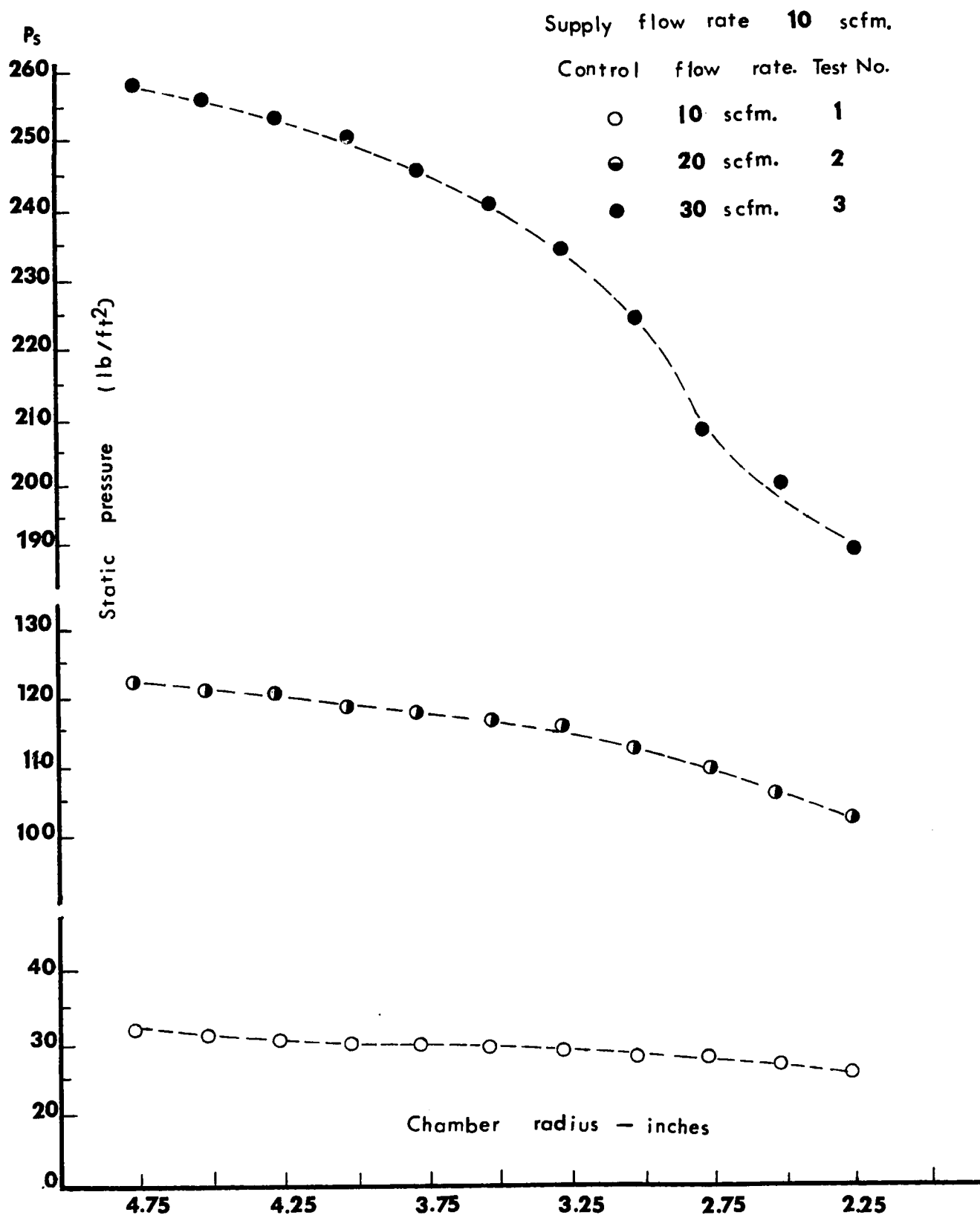
FIG. 26 Static pressure distribution in 10-in dia. chamber.

APPENDIX I

Three-dimensional probes are used to measure yaw and pitch angle, and total and static pressure. United Sensor DAT probes also measure total temperature.

United Sensor three-dimensional probes have five measuring holes. They are used like two-dimensional probes (see Bulletin 4) except that an additional differential pressure, P_4-P_5, is read to indicate pitch angle.

Preferably the probes are rotated until $P_2 = P_3$, and the yaw angle of the stream is then indicated by the take-off block. Pitch angle is determined by calculating $(P_4$-$P_5) / (P_1$-$P_2)$ and using the calibration curve for the individual probe, such as shown as curve A in Fig. 1 or Fig. 2. At this pitch angle θ the velocity pressure coefficient $(P_t$-$P_s) / (P_1$-$P_2)$ and total pressure coefficient $(P_1$-$P_t) / (P_t$-$P_s)$ can be read from curves B and C, and P_t-P_s and P_s calculated.

$(P_t$-$P_s) / (P_1$-$P_2)$ is somewhat sensitive to Mach number, so calibrations are customarily made at two Mach numbers, approximately .2 and .4. For convenience these are expressed in terms of "M_r", where $M_r = (P_t$-$P_s) / P_{tabs}$.

A typical installation with manometers is shown in Figure 3. The choke (USC-1160) is not essential but reduces the balancing time necessary before reading pressures.

At some sacrifice in accuracy, the probes can b used without rotating to balance the yaw pressure P_2 and P_3. The yaw angle (the difference betwee . the direction of flow and the direction indicated b the take-off block) is then indicated by P_2-P_3. A spe cial set of calibration curves must be supplied to permit both yaw angle and pitch angle, as well as stat: and total pressures, to be determined from th observed probes pressures. Further information ma be obt:. ned on request.

FOR MEASURING TOTAL AND STATIC PRESSURES, YAW AND PITCH ANGLES AND TOTAL TEMPERATURE

DA: Five hole, prism shaped measuring section. Measures total and static pressure yaw angle and pitch angle. Furnished with individual calibration curves up to pitch angles of 40°. Tip extends 2 diameters beyond holes. Typical calibration shown in Fig. 1. Smallest size can be inserted through 1/8" hole. Usable up to Mach 0.7.

d = .125", .187", .250", .312", .375"

DAT: Five holes plus thermocouple. Measures total and static pressure, yaw angle, pitch angle, and total temperature. Furnished with individual calibration curves up to pitch angles of 40°. Tip extends 3.5 diameters beyond holes.

d = .187", .250", .312", .375"

DC: Five holes. Measures total and static pressure, yaw angle, and pitch angle. More suitable for use near boundaries than type DA. Furnished with individual calibration curves up to pitch angles of 40°. Usable up to Mach 0.7. DC-120 head fits through clearance hole .62" diameter. Typical calibration curve illustrated in Fig. 2.

d = .125"

Unless otherwise specified, all th above probes are made of corrosion-resistant non-magnetic stainless steel silver brazed. If required, inconel of SAE 310 can be specified. For high temperature use, all probes can be welded except in sizes under .250".
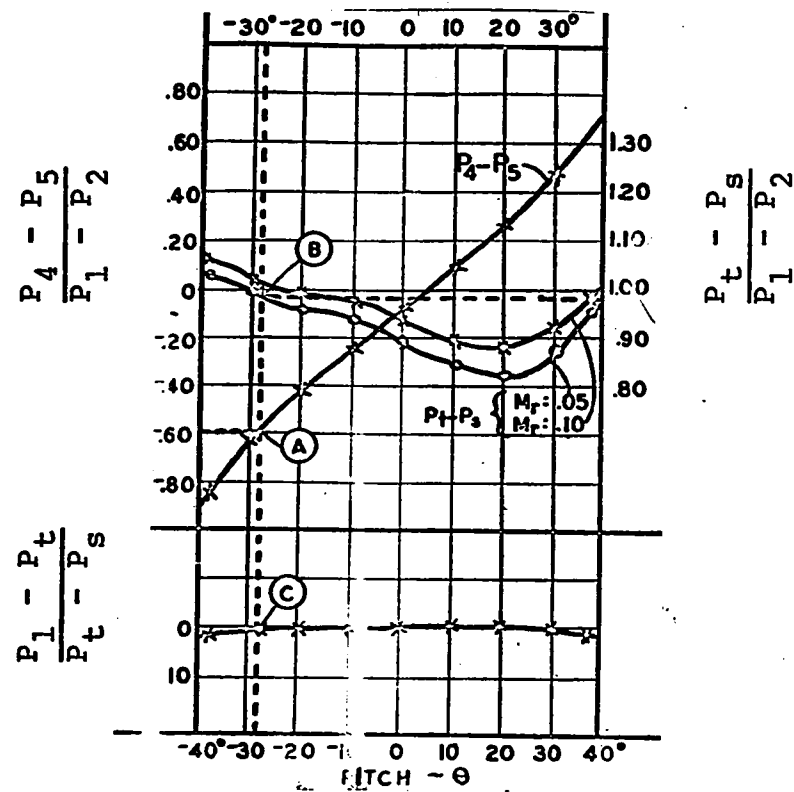
FIG. A.1 Typical calibration of DA probe vs.

$$M_r = \frac{P_t - P_s}{P_{t\ abs}}$$
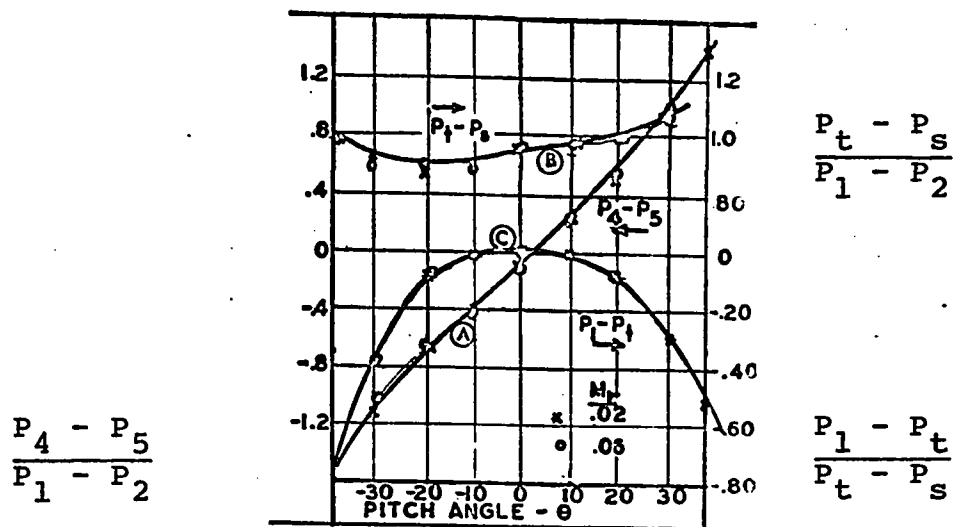
FIG. A.2   Typical calibration of DC probe
vs. M_r and pitch angle.
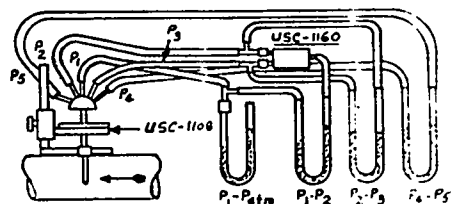
FIG. A.3a   Typical manometer connections
for DA or DC probe.
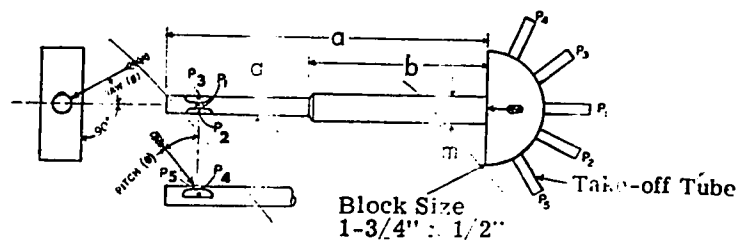
FIG. A.3b   Three-dimensional probe

Indicated static pressure (p_2 or P_3) is more subject to errors in measurement than indicated total pressure (P_1),

Introducing a probe into a small passage immediately changes the static pressure of the passage itself by reducing the cross-sectional flow area. For round probes perpendicular to flow the drop in static pressure at the probe cross-section and downstream from it is approximately:

$$\frac{Ps_1 - Ps_2}{Pt - Ps_1} = 1.2 \frac{a}{A}$$

Where Ps_1 and Ps_2 are original and modified static pressure, Pt is total pressure and $\underline{a}$ is the fraction of passage area (A) blocked by the cross-section of the probe (a).
$\frac{a}{A}$

In addition various errors are covered by Mach Number, Pitch Angle, Yaw Angle, and immersion depth.

Yaw angle errors are zero when the probe is rotated $P_2 = P_3$.

Mach Number errors are shown in the individual calibration charts. Generally the indicated static pressure (P_2 or P_3) increases with Mach Number linearly with the quantity $\frac{Pt - Ps}{Pt}$ abs.

Pitch angle errors are shown on the individual calibration charts. Immersion errors are due to effects of boundaries of the passage and the secondary flow along the upstream edge of the probe which in turn is influenced by the total pressure gradient in the passage.

For general use the probes which are cantilevered out from one side of a passage can be assumed to read true static pressure (subject to the errors listed above) when the holes are 10 probe diameters away from the boundary they project through and the probe tip at least one diameter from the opposite wall.

Probes which extend through both walls can be considered accurate when the holes are at least 5 diameters from either wall.

The accompanying curves show the magnitude of errors when probes are placed near boundaries. For comparison a curve for a standard Pitot-static tube is included. This shows that even this type can read as much as 4% low near a boundary.

Curves are shown for 3" and 8" test passage. All probes up to 3/16" diameter are calibrated at 1.5" immersion in the 3" passage using the wall static pressure at the same cross section as a reference. Larger probes are calibrated in the 8" section.

θ: PITCH ANGLE

−50° −40° −30° −20° −10°   0°   +10° +20° +30° +40° +50°

PITCH ANGLE PRESSURE COEFFICIENT
VS. PITCH ANGLE

VELOCITY PRESSURE COEFFICIENT
VS. PITCH ANGLE

$$\frac{P_4 - P_5}{P_1 - P_2}$$

$$\frac{P_t - P_s}{P_1 - P_2}$$
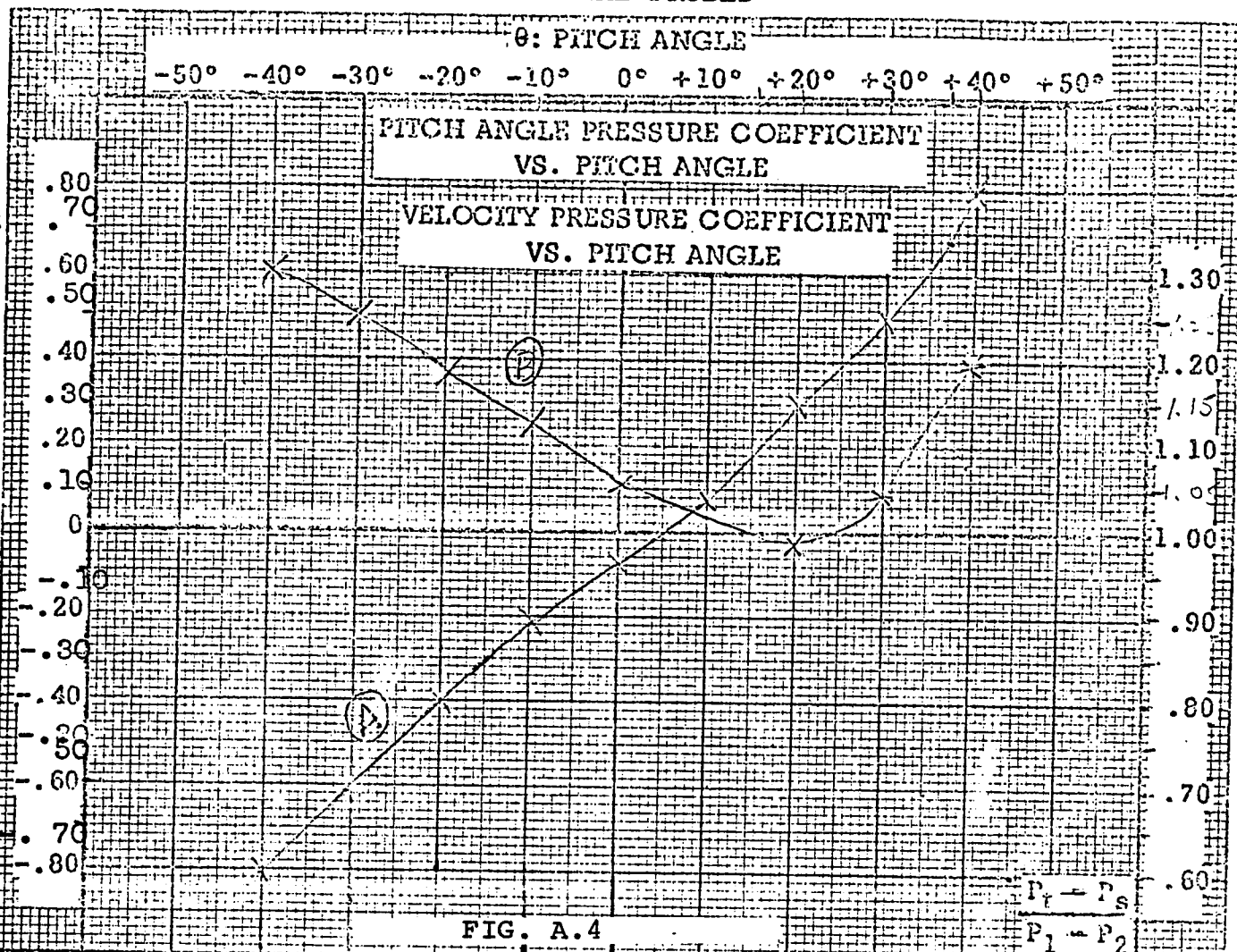
FIG. A.4

$$\frac{P_1 - P_t}{P_t - P_s}$$

TOTAL PRESSURE COEFFICIENT
VS. PITCH ANGLE
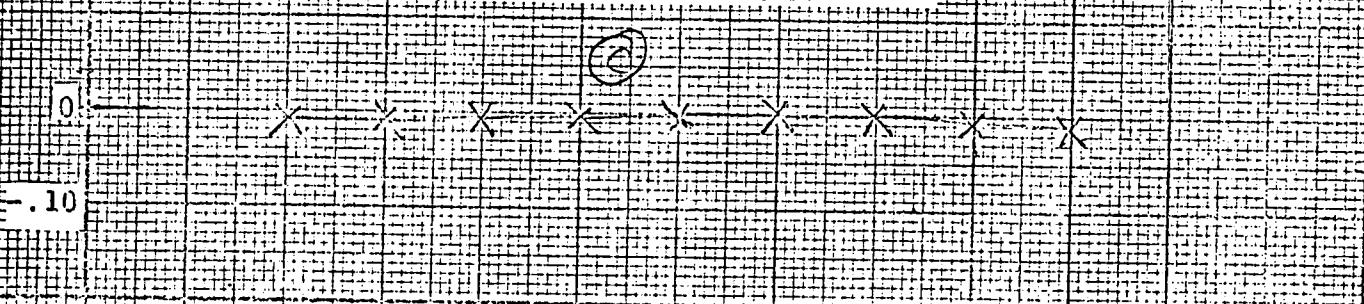
P_t : TOTAL PRESSURE
P_s : STATIC PRESSURE
P_1 : INDICATED TOTAL PRESSURE
P_2 : INDICATED STATIC PRESSURE
P_4, P_5 : PITCH ANGLE PRESSURES

$$M_r : \frac{P_1 - P_2}{P_1 \ abs.}$$

FIG. A.5

θ

& CONTROL CORP.

WATERTOWN · MASS

PROBE TYPE: DA 125
SERIAL NO.: A 761
DATE: 2/9/70
CALIB. BY:
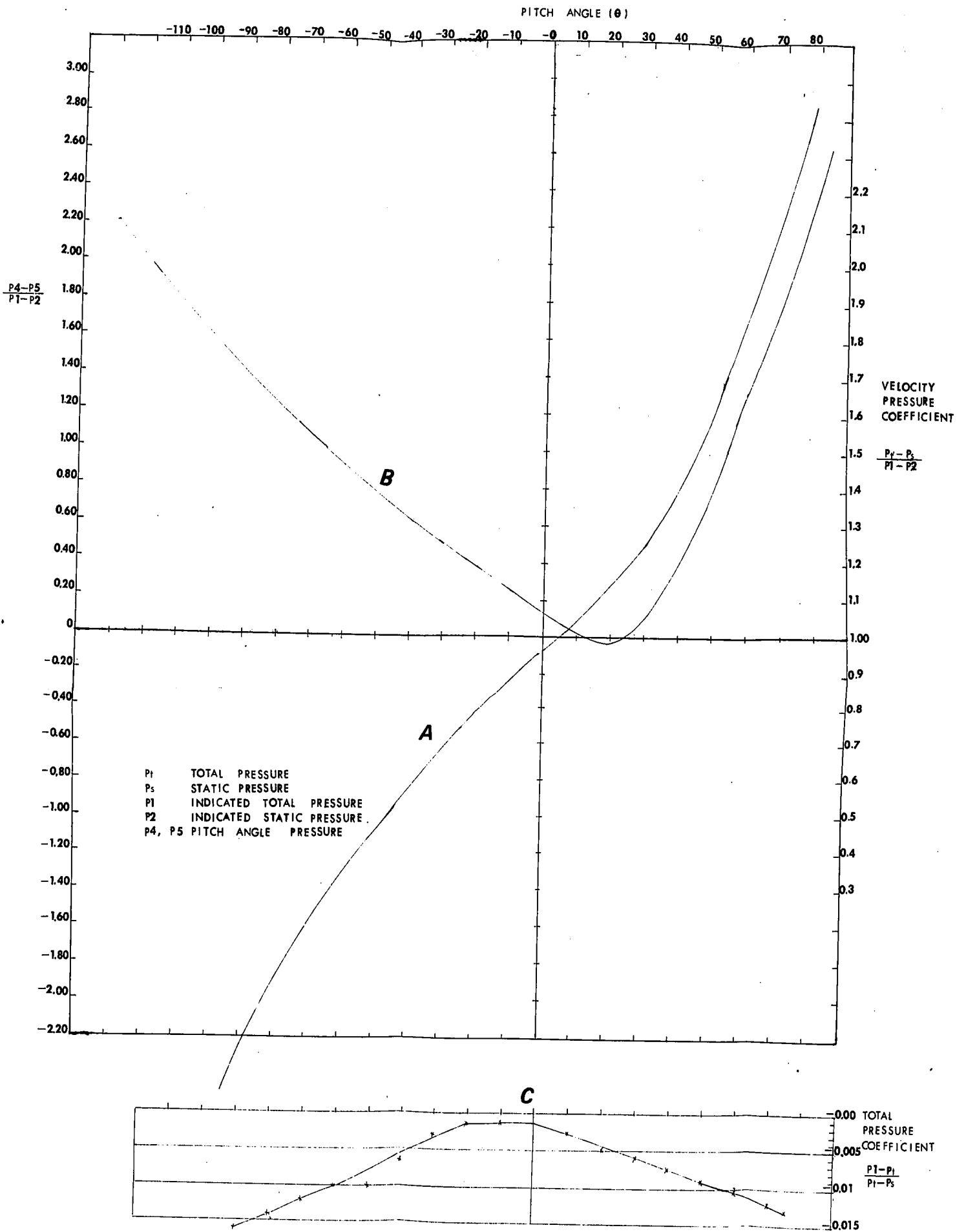
FIG A6   CALIBRATION DATA FOR THREE DIMENSIONAL PROBE

APPENDIX II

VELOCITY COMPONENT TABLES

The flow chart describes the step-by-step procedure showing how the total velocities and their components were found from the experimentally measured pressure values. The tabulated yaw and pitch angles are expressed in degrees and the velocity components in fps. The wall static pressure measurements for different test runs are tabulated on page II-13 in psf units.

APPENDIX II

VELOCITY COMPONENTS TABLES

FLOW CHART OF COMPUTING VORTEX FLOW
VELOCITY COMPONENTS.

```
┌─────────────────────────────────────────────────────┐
│              PROGRAM   CURVE2                         │
│ READ IN  INDICATED   TOTAL  PRESSURE  P1.            │
│          INDICATED  STATIC  PRESSURE  P2, P3.        │
│          PITCH   ANGLE    PRESSURE  P4, P5.          │
│          YAW   ANGLE.                                 │
└─────────────────────────────────────────────────────┘
┌─────────────────────────────────────────────────────┐
│ COMPUTING  VALUE  OF  (P4—P5)/ (P1—P2)      AT       │
│          EACH. STATION.                               │
└─────────────────────────────────────────────────────┘
┌─────────────────────────────────────────────────────┐
│ FIND OUT VELOCITY  COEFFICIENT   CB=(PT—PS)/(P1—P2)  │
│          ON  CURVE  B,  TOTAL  PRESSUE COEFFICIENT   │
│          CC=(P1—PT)/(PT—PS)  ON  CURVE C    AND      │
│          PITCH ANGLE FROM CALIBRATION   CHART.       │
└─────────────────────────────────────────────────────┘
┌─────────────────────────────────────────────────────┐
│              PROGRAM    PTS3                          │
│ SOLVE  THE  SIMUTANEOUS EQUATIONS:                   │
│          CB=(PT—PS)/(P1—P2),                         │
│          CC=(P1—PT)/(PT—PS),                         │
│          WE  GOT   PT  PS  AT  EACH  STATION.        │
└─────────────────────────────────────────────────────┘
┌─────────────────────────────────────────────────────┐
│              PROGRAM    BLKOR4                        │
│ FIND   OUT  THE  ORIGINAL  STATIC  PRESSUE  PS1,     │
│          SINCE  PROBE TIP  INTRODUCED    THE         │
│          STATIC    PRESSUE  CHANGE.                  │
└─────────────────────────────────────────────────────┘
┌─────────────────────────────────────────────────────┐
│              PROGRAM    TOTAL5                        │
│ FROM   PT—PS1, YAW  ANGLE,  PITCH  ANGLE   FIND      │
│          OUT  THE  TOTAL  VELOCITY      AND          │
│          VELOCITY    COMPONENTS.                     │
└─────────────────────────────────────────────────────┘
```

```
      PROGRAM TOTAL5
C
C
C       TO FIND OUT THE VELOCITY COMPONENTS IN A VORTEX
C       FLOW,
      DO 2222 J=1,9
      PRINT 1111
 1111 FORMAT(1H1//)
      PRINT 8, J
    8 FORMAT(30X,4HTEST,2X,I2,2X, 4HDATA//)
      PRINT 1122
 1122 FORMAT(20X, 25HSUPPLY FLOW RATE =   SCFM,///, 20X,
     1 27HCONTROL FLOW RATE =   SCFM,//)
      PRINT 1234
 1234 FORMAT(20X,38HVELOCITY COMPONENTS OF THE VORTEX FLOW//)
      PRINT 110
  110 FORMAT(20X,3HYAW,  4X,5HPITCH, 3X,2HVZ, 5X,2HVR, 5X,
     12HVT, 5X, 1HV,  //)
      DO 100 I=1,12
      READ 10, PTS,YAW,THETA
   10 FORMAT(3F10.3)
C       PT IS INCHES OF WATER HIGH
      PTS = PTS*.812*14.5*144./401.8
      RHO = 0.002378
      SQV = 2.    * PTS/RHO
      V= SQRT(SQV)
      THETAR = THETA*3.14159/180.
      YAWR= YAW*3.14159/180.
      VT = V*SIN(YAWR)
      VZ = V*COS(YAWR)*COS(THETAR )
      VR = V*COS(YAWR)*SIN(THETAR)
   11 FORMAT(15X,I2,6F7.1,//)
      PRINT 11, I,YAW, THETA, VZ, VR, VT, V
  100 CONTINUE
 2222 CONTINUE
      STOP
      END
```

                FORTRAN DIAGNOSTIC RESULTS FOR   TOTAL5

NO ERRORS

    TOTAL5   P   00346   C   00000   D   00000
OBJ,LGO

SIR GEORGE WILLIAMS UNIVERSITY

SUPPLY FLOW RATE = **10** SCFM

CONTROL FLOW RATE = **10** SCFM

VELOCITY COMPONENTS OF THE VORTEX FLOW

	YAW	PITCH	VZ	VR	VT	V
1	50.0	7.9	55.0	7.6	66.2	36.4
2	53.0	-4.0	43.3	-3.4	64.3	80.5
3	50.0	-15.5	35.6	-9.9	61.4	71.7
4	62.0	-23.0	26.0	-11.9	57.2	64.8
5	67.0	-35.3	17.8	-12.6	51.3	55.7
6	73.0	-49.0	10.7	-12.3	53.3	55.7
7	94.0	-74.0	-0.4	2.9	43.8	43.9
8	115.0	-45.5	-9.2	10.4	29.7	32.8
9	135.3	-14.3	-16.9	4.2	17.4	24.6
10	144.0	-1.5	-19.7	.5	14.3	24.3
11	153.0	11.0	-22.3	-4.3	11.6	25.5
12	159.0	13.5	-23.1	-5.5	9.1	25.5

SUPPLY FLOW RATE = **10** SCFM

CONTROL FLOW RATE = **20** SCFM

VELOCITY COMPONENTS OF THE VORTEX FLOW

	YAW	PITCH	VZ	VR	VT	V
1	51.0	5.5	98.3	9.5	121.9	156.9
2	55.0	-0.5	82.3	-13.9	119.2	145.5
3	57.0	-22.0	68.1	-27.5	113.0	134.8
4	62.0	-35.0	40.5	-28.4	93.1	105.4
5	71.0	-49.5	19.2	-22.5	86.0	91.0
6	90.0	-64.0	.0	-0.0	68.1	68.1
7	117.0	-54.0	-11.9	19.0	44.1	49.5
8	134.0	-3.0	-33.0	1.7	34.2	47.5
9	143.0	4.3	-39.0	-5.7	29.7	49.3
10	149.0	7.5	-43.7	-5.8	25.5	51.5
11	155.0	6.5	-46.7	-5.3	21.9	51.8
12	157.0	2.0	-49.2	-1.7	21.2	54.1

SUPPLY FLOW RATE = **10** SCFM

CONTROL FLOW RATE = **30** SCFM

VELOCITY COMPONENTS OF THE VORTEX FLOW

	YAW	PITCH	VZ	VR	VT	V
1	51.0	7.0	140.9	17.3	175.4	225.6
2	54.0	-11.5	123.2	-25.1	173.0	213.8
3	57.0	-25.8	93.9	-45.3	160.5	191.3
4	62.0	-39.3	57.9	-47.3	140.6	159.3
5	77.0	-64.5	11.1	-23.2	111.2	114.1
6	109.0	-62.0	-13.5	25.3	83.3	88.1
7	122.0	-29.3	-36.9	20.7	54.1	68.7
8	140.0	-1.0	-32.9	.6	27.6	43.0
9	147.0	7.6	-63.1	-8.5	41.3	75.9
10	153.0	5.6	-79.3	-9.2	40.7	89.6
11	155.0	5.7	-75.2	-8.9	35.3	83.5
12	159.0	4.5	-77.0	-6.1	29.7	82.3

SUPPLY FLOW RATE = **15** SCFM

CONTROL FLOW RATE = **10** SCFM

VELOCITY COMPONENTS OF THE VORTEX FLOW

	YAW	PITCH	VZ	VR	VT	V
1	50.0	2.0	63.4	8.9	76.3	99.7
2	55.0	-5.3	53.1	-4.9	76.2	93.0
3	60.0	-11.5	40.5	-6.2	71.6	82.7
4	65.0	-16.5	28.4	-8.5	64.5	71.2
5	68.0	-32.5	20.9	-13.3	61.3	66.1
6	75.0	-44.5	9.4	-9.6	51.2	53.0
7	98.0	-66.3	.5	-1.3	39.7	39.7
8	115.0	-46.0	-9.9	10.2	29.1	32.4
9	134.0	50.5	-8.7	-10.6	14.2	19.8
10	148.0	14.5	-20.4	-7.0	13.7	25.9
11	153.0	22.0	-21.4	-9.7	13.1	23.9
12	157.0	21.5	-25.1	-9.9	11.5	29.3

SUPPLY FLOW RATE = **15** SCFM

CONTROL FLOW RATE = **15** SCFM

VELOCITY COMPONENTS OF THE VORTEX FLOW

	YAW	PITCH	VZ	VR	VT	V
1	50.0	-5.6	92.5	14.0	111.5	145.5
2	54.0	-6.3	72.5	-7.9	100.4	124.1
3	57.0	-16.5	62.3	-18.5	100.1	119.3
4	60.0	-25.8	46.7	-22.5	89.8	103.7
5	69.0	-37.0	29.5	-22.3	96.3	103.2
6	77.0	-47.0	10.5	-11.2	66.5	68.3
7	94.0	-83.5	-0.4	3.4	49.6	49.7
8	132.0	-23.0	-23.0	9.9	27.8	37.4
9	142.0	-10.0	-31.1	5.5	24.7	40.1
10	150.0	-20.0	-34.7	12.6	21.3	42.7
11	160.0	-43.0	-30.0	25.8	15.4	45.0
12	161.0	-1.3	-48.5	1.1	16.7	51.3

SUPPLY FLOW RATE = **15** SCFM

CONTROL FLOW RATE = **20** SCFM

VELOCITY COMPONENTS OF THE VORTEX FLOW

	YAW	PITCH	VZ	VR	VT	V
1	50.0	2.5	108.5	16.9	131.0	171.0
2	52.5	-5.0	99.4	-5.7	128.4	162.9
3	55.0	-17.3	63.2	-25.5	124.4	151.9
4	63.0	-24.0	55.4	-29.5	118.0	133.7
5	67.0	-41.0	32.7	-23.4	102.0	110.8
6	83.0	-55.0	5.4	-5.6	82.9	83.5
7	102.0	-72.0	-3.4	11.8	58.5	59.8
8	124.0	-37.0	-23.3	17.9	41.0	50.7
9	139.0	-4.0	-37.4	2.6	32.6	49.7
10	146.0	3.0	-43.5	-2.3	29.3	52.5
11	151.0	3.5	-48.0	-2.0	26.5	54.9
12	157.0	6.0	-51.3	-5.4	21.9	56.0

SUPPLY FLOW RATE = **20** SCFM

CONTROL FLOW RATE = **10** SCFM

VELOCITY COMPONENTS OF THE VORTEX FLOW

	YAW	PITCH	VZ	VR	VT	V
1	50.0	-0.0	67.5	-1.0	80.4	105.0
2	54.0	-5.0	57.7	-6.1	79.8	98.6
3	59.0	-14.5	45.0	-11.6	77.4	90.3
4	63.0	-21.0	34.5	-13.2	72.5	81.3
5	62.0	-32.3	22.7	-14.2	65.2	71.4
6	71.0	-46.5	13.7	-14.4	57.7	61.0
7	75.0	-76.0	2.9	-11.7	45.0	46.5
8	110.0	-21.5	-16.6	6.5	49.0	52.2
9	133.0	30.5	-11.1	-6.5	13.8	18.9
10	140.0	15.0	-13.5	-3.9	11.8	18.4
11	146.0	30.5	-14.4	-5.5	11.7	20.9
12	150.0	23.0	-23.7	-10.0	14.8	29.7

SUPPLY FLOW RATE = **20** SCFM

CONTROL FLOW RATE = **20** SCFM

VELOCITY COMPONENTS OF THE VORTEX FLOW

	YAW	PITCH	VZ	VR	VT	V
1	49.5	7.4	111.1	14.4	131.2	172.5
2	53.0	-6.3	97.8	-10.7	130.6	163.6
3	57.0	-21.0	75.3	-29.1	125.2	149.2
4	61.0	-29.0	57.5	-31.0	116.6	135.6
5	66.0	-42.3	34.0	-30.8	103.0	112.8
6	81.0	-61.8	6.4	-12.0	86.0	87.0
7	101.0	-75.5	-3.0	11.5	61.2	62.4
8	122.0	-47.0	-13.7	20.1	44.0	51.8
9	135.0	-8.0	-39.0	6.3	46.4	57.1
10	147.0	-2.0	-50.5	1.5	32.8	60.2
11	151.0	4.5	-47.2	-3.7	26.2	54.1
12	157.0	1.0	-52.0	-0.9	22.1	56.5

SUPPLY FLOW RATE = **20** SCFM

CONTROL FLOW RATE = **30** SCFM

VELOCITY COMPONENTS OF THE VORTEX FLOW

	YAW	PITCH	VZ	VR	VT	V
1	51.0	8.0	157.5	22.1	196.4	252.7
2	55.0	-5.0	135.8	-21.5	196.3	239.7
3	57.0	-20.5	114.5	-42.9	183.7	225.0
4	61.0	-34.0	78.1	-52.7	169.9	194.3
5	69.0	-47.0	38.5	-41.2	145.9	157.4
6	95.0	-67.3	3.9	-9.4	116.3	116.8
7	109.0	-71.0	-9.0	26.1	80.1	84.7
8	130.0	-23.5	-44.5	19.4	57.8	75.5
9	141.0	-1.0	-59.2	1.0	47.9	76.2
10	149.0	1.5	-69.0	-1.8	41.5	80.5
11	154.0	5.5	-75.4	-6.0	37.1	84.6
12	168.0	2.1	-83.2	-3.1	17.7	85.1

```
        PROGRAM CHAM
C       I IS THE TEST NUMBER, WHEN I=3 OR 9 MERCURY IS USED,
C       OTHERWISE 0.812 SP.WT LIQUID USED.
        PRINT 99
     99 FORMAT (1H1,//)
        PRINT 1122
   1122 FORMAT( 30X, 6HSTATIC,/)
        PRINT 101
    101 FORMAT(  20X, 33HPRESSURE DIST. ACROSS THE CHAMBER//)
        PRINT 102
    102 FORMAT(1X, 4HTEST,1X,2HP1,4X,2HP2,4X,2HP3,4X, 2HP4, 4X,
       12HP5,4X, 2HP6,4X,2HP7, 4X,2HP8,4X,2HP9,4X,3HP10, 3X,3HP11,
       2//)
        DO 1111 I=1,9
        READ 11,P1 ,P2,P3,P4,P5,P6,P7,P8,P9, P10,P11
     11 FORMAT(11F6.2)
        IF(I.EQ.3) GO TO 111
        IF(I.EQ.9) GO TO 111
        CONS = 0.812*14.5*144./401.8
        GO TO 1000
    111 CONS = 13.6 *14.5*144./401.8
   1000 P1=P1*CONS
        P2=P2*CONS
        P3=P3*CONS
        P4=P4*CONS
        P5=P5*CONS
        P6=P6*CONS
        P7=P7*CONS
        P8=P8*CONS
        P9=P9*CONS
        P10=P10*CONS
        P11=P11*CONS
        PTP=PTP*CONS
        PRINT 1,  I, P1,P2,P3,P4,P5,P6,P7,P8,P9,P10,P11
      1 FORMAT( I3, 11F6.1//)
   1111 CONTINUE
        PRINT 1234
   1234 FORMAT(20X, 37HSTATIC PRESSURE IN LB PER SQUARE FEET)
        STOP
        END
```

FORTRAN DIAGNOSTIC RESULTS FOR   CHAM

NO ERRORS

CHAM   P   00376   C   00000   D   00000
OBJ,LGO

PRESSURE DIST. ACROSS THE CHAMBER

TEST	P1	P2	P3	P4	P5	P6	P7	P8	P9	P10	P11
1	25.9	26.9	27.6	28.2	28.6	28.9	29.3	29.7	30.1	30.7	31.4
2	102.1	105.5	108.9	111.8	114.8	116.0	117.3	118.2	119.8	121.1	121.9
3	190.1	199.3	208.5	224.7	233.9	241.0	245.2	249.5	253.0	255.8	257.3
4	28.0	29.0	29.3	29.7	30.1	30.4	30.8	31.1	31.4	32.1	32.5
5	59.1	60.8	62.0	62.9	63.7	64.6	65.4	66.2	67.1	67.5	67.9
6	106.3	109.7	113.1	114.8	119.0	119.8	120.7	121.5	122.4	124.1	125.3
7	30.0	30.6	31.0	31.2	31.6	31.7	32.2	32.6	32.7	33.2	33.3
8	112.2	114.8	117.3	120.3	121.5	123.2	124.9	125.7	126.6	127.4	129.5
9	229.0	237.5	247.4	254.4	261.5	265.7	268.6	274.2	277.0	279.9	282.7

STATIC PRESSURE IN LB PER SQUARE FEET

APPENDIX III

CALCULATION OF STANDARD DEVIATIONS

In order to assess the accuracy and repeatibility
of the experimental measurements, seven different runs of a
particular test condition, where both the supply and control
flow rates were kept at 10 scfm, were carried out. From the
measured data, pitch and yaw angles, as well as total velo-
city, were computed using the same procedures described in
Appendix II and these parameters are expressed in degrees
and fps, respectively.

Following the tabulated data, the arithmetic mean
and standard deviations of total velocity, yaw and pitch
angles were computed for all measuring stations. These
parameters are expressed in fps and degrees, respectively.

In order to express the relative variations of
measured data for different stations, the criteria termed
the "coefficient of variation" developed by Pearson were
used. It is simply the standard deviation as a percentage
of the arithmetic mean. The results for the seven test runs
are tabulated and graphically represented in Figs. A-7 and
A-8.

The maximum coefficients of variation of the total
velocity and yaw angle are in the order of 8% and 2%, res-
pectively. This is extremely good considering the possible
non-symmetry of the flow and the difficulties in measuring
the pressures in the reversed flow region. This is evidenced

from the fact that the maximum coefficient of variation for total velocity occurs in the vicinity of the region where reversed flow starts. Since the absolute magnitude of the velocity will be relatively small in that region, measurement error would probably show up in a more exaggerated manner.

Fig. A-8 shows the coefficient of variation for the pitch angles. For the major part of the measurements, the coefficient of variation is below 10%; however, at stations near the edge of the exit hole, the coefficients of variation become very large. This may be explained by the fact that the edge of the vortex exit hole may have a significant effect on the measurement. Furthermore, the absolute magnitude of the pitch angle is very small. For example, at station 2, the arithmetic mean of the pitch angle is only 2.36 degrees. Consequently, any small error introduced in the measurement, when compared with the actual angle, will be significantly amplified. Even though a figure of 44.3% of the coefficient of variation is indicated, the actual standard deviation is only in the order of one degree.

FLOW CHART OF COMPUTING STANDARD DEVIATION

FIND OUT YAW ANGLE, PITCH ANGLE AND TOTAL VELOCITY AT EACH STATION FOR EACH TEST. SAME PROCEDURE AS STATED IN APPENDIX II WAS USED.

PROGRAM **STDDEV**

READ IN YAW ANGLE, PITCH ANGLE AND TOTAL VELOCITY.

FIND OUT THE AVERAGE VALUES OF YAW ANGLE, PITCH ANGLE AND TOTAL VELOCITY.

$$\bar{x} = \frac{\sum X_i}{N}$$

FIND OUT STANDARD DEVIATION

$$S = \sqrt{\frac{\sum (X_i - \bar{x})^2}{N}}$$

FIND OUT COEFFICIENT OF VARIATION.

$$C.V = \frac{S}{\bar{x}}$$

PLOTTING AND DISCUSSION.

FIG. A7   Location of stations

FIG. A8   Location of stations

```
      PROGRAM STDDEV
      DIMENSION YA(7,12), PA(7,12),V(7,12),AVYA(12),AVPA(12),AVV(12),
     1CVYA(12), CVPA(12),  CVV(12)
C     YA=YAW ANGLE
C     PA=PITCH ANGLE
C     V=TOTAL VELOCITY
C     AVYA=AVERAGE YAW ANGLE
C     AVPA=AVERAGE PITCH ANGLE
C     AVV=AVERAGE VELOCITY
C     I IS THE SET NUMBER OF THE TEST.
C     J IS THE STATION NUMBER OF THE TEST.
      DO 1 I=1,7
      PRINT 345
  345 FORMAT(1H1, //,//)
      PRINT 456,I
  456 FORMAT(23X,  4X,  4HTEST,2X,3H1 =,I2,2X,  4HDATA,//)
      PRINT 1122
 1122 FORMAT(  20X, 24HSUPPLY FLOW RATE=10 SCFM,//,20X,
     126HCONTROL FLOW RATE =10 SCFM,//)
      PRINT 567
  567 FORMAT(10X,7HSTATION,6X,  9HYAW ANGLE,5X,11HPITCH ANGLE,4X,
     18HVELOCITY,//)
      DO 10 J=1,12
      READ 11, YA(I,J), PA(I,J), V(I,J)
   11 FORMAT(3F10.3)
      PRINT 100,J, YA(I,J), PA(I,J), V(I,J)
   10 CONTINUE
    1 CONTINUE
CC    TO FIND AVERAGE VALUE AT EACH STATION.
  222 FORMAT(1H1//)
      PRINT 222
      PRINT 323
  323 FORMAT(20X, 29HAVERAGE VALUE AT EACH STATION,//)
      PRINT 555
  555 FORMAT(10X,7HSTATION,6X,  9HYAW ANGLE,6X,11HPITCH ANGLE,4X,
     18HVELOCITY,//)
      DO 1001 J=1,12
      SUMYA=0.
      SUMPA=0.
      SUMV=0.
      DO 101 I=1,7
      SUMYA=SUMYA+YA(I,J)
      SUMPA=SUMPA+PA(I,J)
      SUMV=SUMV + V(I,J)
  101 CONTINUE
      AVYA(J) = SUMYA/7.
      AVPA(J) = SUMPA/7.
      AVV(J)= SUMV/7.
      PRINT 100, J, AVYA(J), AVPA(J), AVV(J)
  100 FORMAT(10X, I3, 3(5X,F10.2   ),//)
 1001 CONTINUE
CC    TO FIND OUT THE STANDARD DEVIATION AT EACH STATION.
      SSEYA=0.
      SSEPA=0.
```

```
        SSEV=0.
        PRINT 345
        PRINT 322
    322 FORMAT(25X, 18HSTANDARD DEVIATION,
       1                              //, 10X, 7HSTATION,10X,
       2 9HYAW ANGLE,5X,  11HPITCH ANGLE,5X,   8HVELOCITY,//)
        DO 88 J=1,12
C
C       SQRSYA=SQAURE SUM OF YAW ANGLE
C
        SQRSYA= (AVYA(J) -YA(1,J))**2 + (AVYA(J) -YA(2,J))**2 + (AVYA(J)
       1-YA(3,J))**2+(AVYA(J) - YA(4,J))**2 + (AVYA(J)-YA(5,J))**2 +
       2(AVYA(J) -YA(6,J))**2   +(AVYA(J)-YA(7,J))**2
C       SQRSPA= SQUARE SUM OF THE PITCH ANGLE
C
        SQRSPA = (AVPA(J) - PA(1,J))**2 + (AVPA(J) - PA(2,J))**2 +
       1(AVPA(J) -PA(3,J))**2 + (AVPA(J)-PA(4,J))**2+ (AVPA(J)- PA(5,J))
       2**2 + (AVPA(J) - PA(7,J))**2
C       SQRSV= SQUARE SUM OF THE VELOCITY
C
        SQRSV = (AVV(J) -V(1,J))**2 + (AVV(J) - V(2,J))**2 +
       1(AVV(J) - V(3,J))**2 + (AVV(J) - V(4,J))**2 + (AVV(J) - V(5,J))
       2**2 + (AVV(J) - V(6,J))**2 + (AVV(J) - V(7,J))**2
C
C       SEYA IS THE STANDARD DEVIATION OF YAW ANGLE.
C       SEPA IS THE STANDARD DEVIATION OF PITCH ANGLE.
C       SEV IS THE STANDARD DEVIATION OF VELOCITY.
        SQRSYA=SQRSYA/7.
        SQRSPA=SQRSPA/7.
        SQRSV=SQRSV/7.
        SEYA=SQRT(SQRSYA)
        SEPA=SQRT(SQRSPA)
        SEV =SQRT(SQRSV)
C       TO FIND OUT THE COEFFICIENT OF VARIATION.
        CVYA(J) = SEYA/ABS(AVYA(J)   )
        CVPA(J) =SEPA/ABS(AVPA(J) )
        CVV(J) = SEV/ABS(AVV(J) )
    134 FORMAT(10X, I3,10X,3(F10.3,5X)//)
        PRINT 134, J,SEYA,SEPA, SEV
C       TO FIND OUT THE AVERAGE STANDARD DEVIATIONS.
        SSEYA=SSEYA+SEYA
        SSEPA=SSEPA+ SEPA
        SSEV=SSEV + SEV
     88 CONTINUE
        SSEYA=SSEYA/12.
        SSEPA=SSEPA/12.
        SSEV=SSEV/12.
        PRINT 1111, SSEYA,  SSEPA,  SSEV
   1111 FORMAT(//,10X,7HAVERAGE, 6X, 3(F10.3, 5X))
        PRINT 222
        PRINT 321
    321 FORMAT( 25X,  24HCOEFFICIENT OF VARIATION.//)
        PRINT 555
        COYA=0.
```

```
FORTRAN (3.2)/MASTER

      COPA= 0.
      COV=0.
      DO 333 J=1,12
      CVYA(J)= CVYA(J)*100.
      CVPA(J) = CVPA(J)*100.
      CVV(J) = CVV(J)*100.
      PRINT 134, J, CVYA(J), CVPA(J), CVV(J)
      COYA=COYA + CVYA(J)
      COPA= COPA + CVPA(J)
      COV = COV + CVV(J)
  333 CONTINUE
      COYA = COYA/12.
      COPA=COPA/12.
      COV= COV/12.
      PRINT 1111, COYA, COPA, COV
      STOP
      END
```

FORTRAN DIAGNOSTIC RESULTS FOR   STDDEV

NO ERRORS

    STDDEV   P   02447   C   00000   D   00000
OBJ,LGO

SIR GEORGE WILLIAMS UNIVERSITY

TEST 1 - 1 DATA

SUPPLY FLOW RATE=10 SCFM

CONTROL FLOW RATE =10 SCFM

STATION	YAW ANGLE	PITCH ANGLE	VELOCITY
1	59.00	7.90	46.34
2	53.00	-4.00	40.56
3	39.00	-15.50	71.68
4	42.00	-23.00	64.54
5	57.00	-35.30	55.69
6	73.00	-44.00	43.93
7	74.00	-74.00	32.54
8	115.00	-43.50	24.63
9	135.00	-14.00	24.35
10	144.00	-1.50	25.52
11	153.00	11.00	25.47
12	159.00	13.50	25.99

TEST 1 - 2 DATA

SUPPLY FLOW RATE=10 SCFM

CONTROL FLOW RATE =10 SCFM

STATION	YAW ANGLE	PITCH ANGLE	VELOCITY
1	52.00	10.50	85.93
2	55.00	-1.50	82.10
3	56.00	-15.50	76.60
4	62.00	-21.50	68.11
5	68.00	-32.50	59.14
6	74.00	-48.00	46.90
7	97.00	-72.50	34.55
8	113.00	-49.25	20.53
9	135.00	-13.25	25.05
10	142.00	-1.50	25.52
11	134.00	11.00	26.13
12	132.00	13.50	25.99

TEST 1 - 3 DATA

SUPPLY FLOW RATE=10 SCFM

CENTRAL FLOW RATE =10 SCFM

STATION	YAW ANGLE	PITCH ANGLE	VELOCITY
1	50.00	13.50	95.57
2	53.00	-2.50	79.37
3	57.00	-14.50	73.82
4	62.00	-23.50	65.29
5	65.00	-33.00	57.71
6	73.00	-48.25	45.92
7	93.00	-73.00	30.16
8	115.00	-43.00	21.18
9	135.00	-13.13	22.57
10	143.00	-1.00	26.90
11	154.00	13.50	26.03
12	159.00	14.50	24.60

TEST 1 - 4 DATA

SUPPLY FLOW RATE=10 SCFM

CONTROL FLOW RATE =10 SCFM

STATION	YAW ANGLE	PITCH ANGLE	VELOCITY
1	50.00	11.50	83.74
2	54.00	-1.50	79.58
3	57.00	-13.25	75.41
4	62.00	-23.00	65.14
5	65.00	-34.63	57.56
6	73.00	-44.00	55.30
7	92.00	-72.75	32.71
8	117.00	-41.30	21.64
9	135.00	-13.13	22.57
10	140.00	-2.00	24.41
11	142.00	13.50	26.03
12	135.00	13.50	25.99

SIR GEORGE WILLIAMS UNIVERSITY

TEST 1 - 5 DATA

SUPPLY FLOW RATE=10 SCFM

CONTROL FLOW RATE =10 SCFM

STATION	YAW ANGLE	PITCH ANGLE	VELOCITY
1	44.00	3.92	85.70
2	54.05	-1.50	85.20
3	57.70	-12.40	79.35
4	61.00	-21.45	69.90
5	65.60	-33.50	60.38
6	72.40	-47.25	48.30
7	92.00	-73.00	35.84
8	113.40	-44.30	21.64
9	136.00	-16.25	22.79
10	144.00	-1.32	26.22
11	133.00	11.25	25.45
12	154.00	13.40	25.32

TEST 1 - 6 DATA

SUPPLY FLOW RATE=10 SCFM

CONTROL FLOW RATE=10 SCFM

STATION	YAW ANGLE	PITCH ANGLE	VELOCITY
1	45.00	11.75	86.76
2	52.00	-1.50	81.65
3	53.00	-13.00	77.30
4	55.00	-23.50	58.74
5	56.00	-34.94	58.74
6	72.00	-51.50	46.83
7	45.00	-73.30	31.08
8	110.00	-79.00	24.70
9	135.00	-14.50	26.67
10	145.00	-1.00	26.89
11	143.00	11.00	26.13
12	150.00	13.50	25.99

TEST 1 - 7 DATA

SUPPLY FLOW RATE=10 SCFM

CONTROL FLOW RATE =10 SCFM

STATION	YAW ANGLE	PITCH ANGLE	VELOCITY
1		7.40	76.98
2	52.00	-4.00	80.56
3	58.00	-18.00	71.55
4	53.00	-22.25	64.76
5	54.00	-34.78	49.43
6	73.00	-44.00	43.93
7	54.00	-77.40	32.15
8	115.00	-42.25	25.22
9	134.00	-15.25	25.05
10	146.00	-1.31	26.22
11	153.00	11.00	26.13
12	154.00	13.50	25.32

AVERAGE VALUE AT EACH STATION

STATION	YAW ANGLE	PITCH ANGLE	VELOCITY
1	50.00	16.27	96.00
2	53.29	-6.36	81.29
3	57.71	-14.11	75.10
4	61.57	-22.64	65.35
5	65.57	-34.09	56.95
6	73.14	-44.90	47.30
7	83.29	-73.71	32.73
8	114.55	-67.60	22.79
9	135.43	-13.93	24.15
10	144.24	-1.33	26.01
11	153.29	11.75	25.91
12	156.26	13.75	25.60

STANDARD DEVIATION

STATION	YAW ANGLE	PITCH ANGLE	VELOCITY
1	.426	1.902	1.031
2	1.083	1.044	1.842
3	1.161	1.196	2.702
4	.724	.744	3.244
5	.725	.049	3.356
6	.634	.755	3.536
7	1.756	1.563	1.799
8	1.355	2.424	1.824
9	.737	1.041	1.457
10	1.161	.225	.715
11	.452	1.073	.288
12	.233	.335	.502
AVERAGE	.937	1.109	1.862

STATION	YAW ANGLE	PITCH ANGLE	VELOCITY
1	1.852	18.526	1.199
2	1.933	44.270	2.266
3	2.011	8.475	3.598
4	1.183	3.285	4.963
5	1.111	2.783	5.893
6	.873	1.543	7.580
7	1.876	2.120	5.496
8	1.180	5.071	8.002
9	.538	7.476	6.032
10	.804	20.728	2.747
11	.295	9.134	1.110
12	.524	2.444	1.962
AVERAGE	1.182	10.488	4.237